Controlled bi-functionalization of silica microbeads through grafting of amidoxime/methacrylic acid for Sr(II) enhanced sorption

Yuezhou Wei, Makpal Rakhatkyzy, Khalid A.M. Salih, Kaituo Wang, Mohammed Hamza, Eric Guibal

Controlled bi-functionalization of silica microbeads through grafting of amidoxime/methacrylic acid for Sr(II) enhanced sorption

Yuezhou Wei[a,b,1], Makpal Rakhatkyzy[a,2], Khalid A.M. Salih[a,3], Kaituo Wang[a,5], Mohammed F. Hamza[a,c,*,4], Eric Guibal[d,*,6]

[a] Guangxi Key Laboratory of Processing for Non-ferrous Metals and Featured Materials, School of Resources, Environment and Materials, Guangxi University, Nanning 530004, PR China
[b] Shanghai Jiao Tong University, Shanghai, PR China
[c] Nuclear Materials Authority, POB 530, El-Maadi, Cairo, Egypt
[d] Polymers Composites and Hybrids (PCH), IMT Mines Ales, Alès, France

HIGHLIGHTS

- Bi-functionalization of silica particles increases Sr(II) sorption properties.
- Methacrylic (80%)/amidoxime (20%) substitution ratio is optimum.
- Maximum sorption capacity reaches 1.57 mmol Sr g^{-1} at pH 8.
- Total Sr(II) desorption and weak loss in sorption properties at the fifth recycling.
- The sorbent is remarkably selective to Sr(II) in seawater.

GRAPHICAL ABSTRACT

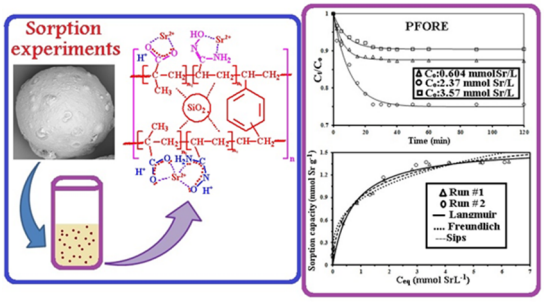

ABSTRACT

Silica microspheres are functionalized through the grafting of either polymethacrylic acid or amidoxime groups (mono-functional composite, PMAA/SiO_2 and PAO/SiO_2, respectively) or in combination (bi-functional composite, PAO_xMAA_{100-x}/SiO_2). The materials are characterized by textural analysis, TGA, SEM-EDX, elemental analysis, FTIR, XPS, pH_{PZC} in order to confirm the synthesis route, identify the reactive groups and support the interpretation of sorption mechanisms toward Sr(II). The sorption of Sr(II), at optimum pH 8, involves amine groups and hydroxyl/carboxyl groups in the bi-functional composite sorbent. The comparison of sorption properties shows that maximum sorption requires a majority of carboxylic groups from polyacrylic compared with amidoxime functions; optimum formulation: $PAO_{20}MAA_{80}/SiO_2$ sorbent. Sorption isotherms are efficiently fitted by the Langmuir and Sips equations: the maximum sorption capacity reaches around 1.38 mmol Sr g^{-1}. Kinetic profiles for sorption are modeled using the pseudo-first order rate equation; equilibrium is achieved within 40–60 min. Complete desorption of Sr(II) using 1 M HCl solutions is even faster; equilibrium time being

Keywords:
Bi-functionalized silica composite
Strontium sorption isotherms
Uptake kinetics
Metal desorption
Sorbent recycling
Mechanism interpretation

* Corresponding authors.
E-mail addresses: yzwei@gxu.edu.cn (Y. Wei), mak_rakh@mail.ru (M. Rakhatkyzy), Immortaltiger7@gmail.com (K.A.M. Salih), wangkaituo@gxu.edu.cn (K. Wang), m_fouda21@hotmail.com (M.F. Hamza), eric.guibal@mines-ales.fr (E. Guibal).
[1] ORCID: 0000-0003-3821-9078.
[2] ORCID: 0000-0001-6365-8916.
[3] ORCID: 0000-0001-6117-6753.
[4] ORCID: 0000-0002-8935-6884.
[5] ORCID: 0000-0002-6756-8413.
[6] ORCID: 0000-0002-2767-6305.

15–20 min. The sorbent can be recycled for 5 cycles with a limited decrease in the sorption performance, and full desorption. In fixed-bed column, the breakthrough curves are fitted by the Thomas equation. In multi-component solutions, the sorbent shows a preferred selectivity according the sequence: K(I) > Ba(II) > Na(I) > Ca(II). Tested on seawater, the sorbent shows high distribution ratio for Sr(II), B(III) and Mo(VI)

1. Introduction

The removal of strontium from water bodies has recently retained increasing attention from scientific community due to Fukushima Daiichi NPP accident [1,2]. The dissemination of radioactive strontium may cause serious health and life hazards due to accumulation in soils [3] and bioaccumulation in the food chain [4]. Apart this accidental dispersion of hazardous ^{90}Sr, the metal is used in fireworks, optical materials including TV tube monitor, ferrite magnets, ceramics and the manufacturing of some toothpastes [5]. Majors threats for human health concern direct radiotoxicity (after nuclear accident), bones diseases (associated with Ca replacement with Sr) causing different types of cancer, anemia, and leukemia [5].

Precipitation coupled with microfiltration has been investigated for the recovery of Sr(II) [6,7]. Solvent extraction was also used [8,9]. However, sorption processes have retained much more attention, playing with a wide diversity of supports. Carbon-based sorbents have been investigated for Sr(II) uptake from surface waters [10–13]. Biosorbents and biopolymers showed also promising properties for strontium uptake. [14-18]. Zeolite, silica and clays have been used under their raw form [19-22], after chemical modification [23-27], magnetite incorporation [5,28], or extractant impregnation [29]. Sorbents impregnated with Prussian Blue and analogues have also been successfully tested for Sr(II) removal [30,31]. Metal and bi-metallic nanoparticles have been applied to the recovery of cesium and strontium from simulated effluents contaminated with radioelements [32,33]. Functionalized polymer resins were widely investigated for Sr(II) recovery [34-36].

Composite organic/inorganic resins have shown promising perspectives combining the mechanical stability of silica core (for example) and highly reactive and selective functionalities of the polymer layer (which can be tailored for specific metal target) [27]. In the case of Sr(II) sorption, the coating of silica core may be based on the grafting of polymers bearing carboxylic-acid moieties [27] (maximum sorption capacity, q_m: increased with temperature up to 92 mg Sr g^{-1}). Indeed, carboxylic acid groups proved being efficient in enhancing the sorption properties of different supports [37] (q_m: 58.5 mg Sr g^{-1}), including directly on carboxylate groups of alginate beads [38] (q_m: 110 mg Sr g^{-1}). Amidoxime reactive groups have also shown high affinity for Sr (II) on synthetic polymers [39], on chitosan-based supports (q_m: 153 mg Sr g^{-1}, [40]) or composite algal/PEI beads (q_m: 189 mg Sr g^{-1}, [41]). Several studies over the last decades have demonstrated the benefits of bi-functionality on metal sorption properties [42–51]. In the case of sulfonic/carboxylic resin, Younis et al. [43] reported sorption capacities as high as 175 mg Sr g^{-1}. This work contributes to the development of bi-functional sorbents for the sorption of Sr(II). Silica particles are coated with polymethacrylic acid (PMAA/SiO_2), polyacrylonitrile (PAN/SiO_2), or amidoximated polyacrylonitrile (PAO/SiO_2) (mono-functionalized silica); the sorption properties are compared with a series of bi-functionalized silica composite (with different fractions of methacrylic acid and amidoxime moieties, PAO_xMAA_{100-x}/SiO_2).

The major outcomes of this work consist of the synthesis of mechanically stable sorbents (based on silica core), with enhanced reactivity (due to the combined effects of methacrylic acid and amidoxime bifunctionality). The optimization of the ratio of reactive moieties brings new insights in the promising perspectives opened by bi-functionality.

In the first part of the work, the materials are characterized using BET and TGA analysis, elemental analysis, FTIR and XPS spectroscopies, and titration (for the determination of pH_{PZC}). In the second part of the work, the sorption of Sr(II) is investigated through the study of pH effect, uptake kinetics, sorption isotherms, metal desorption and sorbent recycling, and sorption in multi-component solutions (sorption selectivity) in batch reactors. The effect of flow rate on Sr(II) sorption in dynamic system (fixed-bed columns) is also investigated. Finally, $PAO_{20}MAA_{80}/SiO_2$ composite sorbent is tested for the removal of Sr(II) from seawater; in an attempt to simulate the recovery of ^{90}Sr(II) from radioactive contaminated effluent.

2. Materials and methods

2.1. Materials

Strontium nitrate, potassium peroxydisulfate, sodium pyrosulfite, ethanol (absolute), sodium carbonate anhydrous, and salts of barium chloride dihydrate ($BaCl_2{\cdot}2H_2O$), potassium chloride (KCl), sodium chloride (NaCl) and anhydrous calcium chloride ($CaCl_2$), used for preparing multi-component solutions, were supplied by Guangdong Guanghua Sci-Tech Co., Ltd., Shantou, Guangdong, China. Stock solutions were prepared at the concentration of 1 g L^{-1} using ultrapure water (UPW). Working solutions were diluted to the assigned concentration using UPW just before use. Hydroxylammonium chloride, methyl cellulose (MC) and polyvinyl alcohol (PVA) were purchased from Shanghai Test Sihewei Chemical Co., Ltd. (Shanghai, China). Silica micro-beads were supplied by Asahi Chemicals, Co Ltd. (Osaka, Japan). Acrylonitrile (AN), divinylbenzene (DVB), nitric acid and hydrochloric acid were purchased from Sinopharm Chemical Reagent Co., Ltd (Shanghai, China).

Seawater for testing Sr(II) removal from complex solutions was collected from Fangchenggang, a prefecture-level city in the south of Guangxi Zhuang Autonomous Region, People's Republic of China, is located at the following coordinates: 21°36′N 108°18′E (see MAP AM1, in Additional Material Section).

2.2. Synthesis of sorbents

2.2.1. Mono-functionalized/SiO_2 sorbent

2.2.1.1. Synthesis of polyacryl-amidoxime/SiO_2 sorbent. A three-necked round bottom flask, heated using a silicone oil bath, was equipped with a condenser and a mechanical stirrer, while the third necked was connected to a dropping funnel. For reducing synthesis costs, experimental conditions were adapted: water was used as the solvent in the polymerization reaction, while $K_2S_2O_8$ and $Na_2S_2O_5$ were selected as redox initiator.

2.2.1.1.1. Synthesis of polyacrylonitrile/SiO_2 sorbent – PAN/SiO_2 (Scheme 1a). The initiator solution was prepared by dissolving 0.5 g $K_2S_2O_8$ and 0.2 g $Na_2S_2O_5$ in 10 mL UPW, under strong stirring, for 20 min at 22 ± 2 °C. Ten grams of porous silica particles were immersed in the mixture of 50 mL PVA solution (1% w/w) and 6 mL MC solution (0.5% w/w), under strong stirring (250 ± 5 rpm). In a second step, the suspension was drop wisely added to the solution containing both the crosslinker and the mixture of monomers (i.e., 1.4 g AN + 0.23 g of DVB). The reaction was maintained for 20 min at 40 °C, before increasing the temperature to 70 °C for 2 h; the final step took place at 90 °C for 7 h. The final product, polyacrylonitrile/SiO_2 (PAN/SiO_2), was obtained after washing with hot water, acetone, and dried at 50 °C under vacuum for 12 h.

2.2.1.1.2. Synthesis of polyacryl-amidoxime/SiO_2 sorbent – PAO/SiO_2

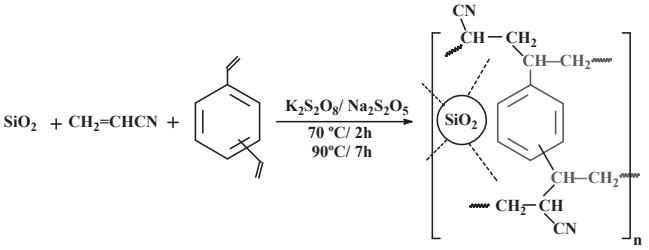

Scheme 1a. Synthesis route for the preparation of PAN/SiO_2.

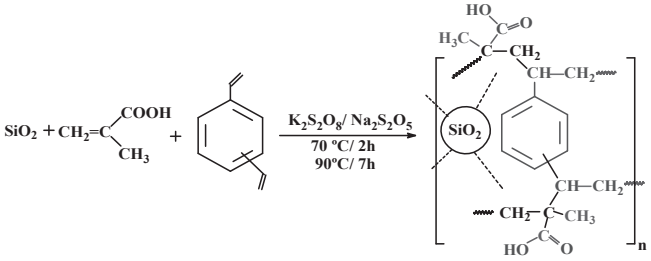

Scheme 2. Synthesis route for the preparation of PMAA/SiO_2.

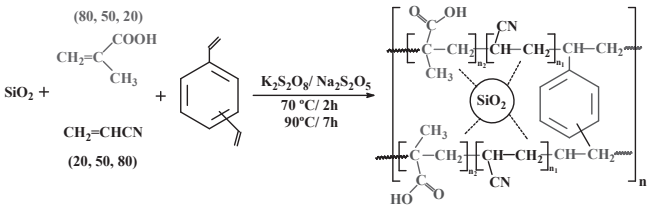

for PAN_{20}/MAA_{80}, PAN_{50}/MAA_{50}, and PAN_{80}/MAA_{20}, respectively.

Scheme 3. Synthesis route for the preparation of PAN_xMAA_{100-x}/SiO_2.

(*Scheme 1b*). Four grams of PAN/SiO_2 were dispersed into 40 mL of water/ethanol mixture (1:1, v/v). Fifteen g of hydroxylammonium chloride were dissolved in 100 mL of water/ethanol solution (5:1, v/v) containing 7 g of Na_2CO_3. This solution was mixed with PAN/SiO_2 suspension for 20 min at 40 °C, before heating under reflux at 70 °C for 5 h. The final product (PAO/SiO_2) was dried under vacuum for 12 h.

2.2.1.1.3. Synthesis of polymethacrylic acid/SiO_2 sorbent – PMAA/SiO_2 (Scheme 2). The synthesis followed exactly the same procedure as described above substituting acrylonitrile with methacrylic acid. The same ratios of monomers to additives were respected. Scheme 2 reports the synthesis route (for polymethacrylic acid (PMAA) functionalization).

2.2.2. Bi-functionalized/SiO_2 sorbent

2.2.2.0.1. Synthesis of polyacrylonitrile/methacrylic acid sorbent with different ratios (Scheme 3). The bi-functionalization of SiO_2 was processed first by simultaneously grafting PAN and PMAA moieties. Ten g of silica micro-beads were mixed with 50 mL of PVA solution (1%, w/w) completed with MC solution (6 mL, 0.5% w/w), followed by dropwise addition of 0.5 g $K_2S_2O_8$ and 0.2 g $Na_2S_2O_5$ (previously dissolved in 10 mL of water). The mixture was stirred (250 ± 5 rpm) at room temperature (i.e., 22 ± 2 °C) for 20 min. The grafting of additional reactive groups was performed by dropwise addition of variable amounts of AN (i.e., 0.3 g, 0.7 g and 1.2 g) and MAA (i.e., 1.2 g, 0.7 g and 0.3 g) in the presence of 0.25 g of DVB. The reaction was thermally processed in three steps: at 40 °C for 20 min, followed by 2 h at 70 °C and finished at 90 °C for 7 h. The copolymer ratios varied to produce: PAN_{20}/MAA_{80}, PAN_{50}/MAA_{50}, and AN_{80}/MAA_{20} respectively. The products (PAN_xMAA_{100-x}/SiO_2) were washed with hot water, acetone, before being dried at 50 °C under vacuum for 12 h.

2.2.2.1. Synthesis of polyacryl-amidoxime/methacrylic acid sorbent with different ratios. The three samples of PAN_xMAA_{100-x}/SiO_2 were amidoximated by reaction with hydroxyl ammonium hydrochloride at 70 °C for 5 h, in the presence of sodium carbonate. Four g of polymer/SiO_2 composite were dispersed into a 1:1 water/ethanol solution (40 mL) before adding $NH_3OH{\cdot}Cl/Na_2CO_3$ (dissolved in 5:1 water/ethanol solution) with the following mass ratios 12:4.8 g, 7.5:3 g; and 3:1.2 g for PAN_{20}/MAA_{80}, PAN_{50}/MAA_{50}, and PAN_{80}/MAA_{20}, respectively. The reaction was initiated at 40 °C, for 20 min. In a second step, the temperature was raised to 70 °C (under reflux) and the reaction lasted for 5 h. Sorbents were filtered off and washed several times with hot water and ethanol and finally dried under vacuum at 50 °C for 12 h. Scheme 4 summarizes the synthesis route (including the generic formula of PAO_xMAA_{100-x} sorbent).

2.3. Characterization of materials

The morphology of sorbent particles was observed using a Phenom ProX scanning electron microscope (SEM, Thermo Fisher Scientific, Netherlands). Semi quantitative EDX analysis (integrated in the SEM equipment) was used for characterizing the sorbents before and after metal sorption. Textural investigation was performed using Micromeritics TriStar II (Norcross, GA, USA); the samples were degassed for 13 h at 100 °C. The specific surface area was determined using BJH methods for BET equation (on both sorption and desorption branches of nitrogen isotherm).

Chemical characterization was investigated using FTIR spectrometry (4000–400 cm^{-1}) with an IRTracer-100 (Shimadzu, Tokyo, Japan). Dried samples were grinded and mixed with KBr and conditioned as KBr disc, prior to FTIR analysis. XPS analysis was performed using an ESCALAB 250XI+ instrument (Thermo Fischer Scientific, Inc., Waltham, MA, USA). Elemental analysis was carried out using a Vario EL cube element analyzer (Elementar Analysensysteme GmbH, Langenselbold, Germany) for quantification of C, H, and N elements in the sorbents. Thermal analysis of the sorbents (PAN_{20}/MAA_{80} and PAO_{20}/MAA_{80})/SiO_2 were performed using a Netzsch STA 449 F3

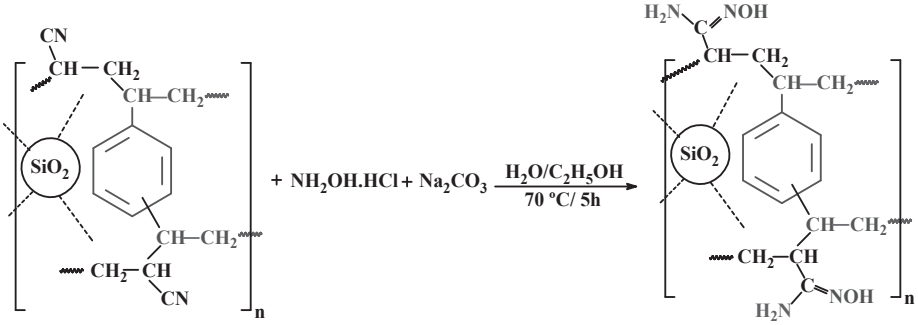

Scheme 1b. Synthesis route for the preparation of PAO/SiO_2.

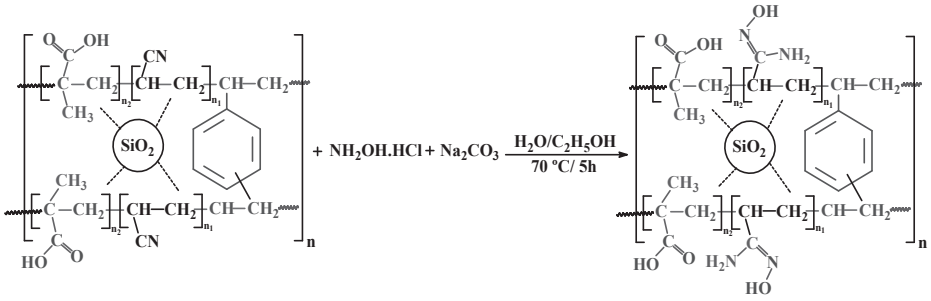

Scheme 4. Synthesis route for the preparation of PAO_xMAA_{100-x}/SiO_2.

Jupiter (NETZSCH-Gerätebau GmbH, Selb, Germany) (temperature ramp: 10 °C/min) under nitrogen atmosphere.

The pH-drift method was used for determining the pH_{PZC} value [52]. A fixed amount of sorbent (i.e., 100 mg) was dispersed under agitation for 48 h in a series of flasks containing 50 mL of 0.1 M or 1 M NaCl solutions with initial pH (pH_0) adjusted to 1–14. The final pH (pH_{eq}) was measured using a Mettler Toledo pH-meter (Colombus, USA) and the pH_{PZC} was determined by the value corresponding to: $pH_0 = pH_{eq}$.

2.4. Sorption studies

Most of the experiments were carried out in batch process. A fixed amount of sorbent (m, g) was mixed with a given volume of solution (V, L), containing strontium (C_0, mmol Sr L^{-1}) for 48 h. The sorbent dosage (SD, g L^{-1}) was defined as SD = m/V. The standard temperature was 22 ± 2 °C and the agitation speed was 170 rpm. The samples were collected at the end of the experiments, before being filtrated on 1.2 µm pore size filter membranes. The residual concentration in the solution (C_{eq}, mmol L^{-1}) was analyzed using ICP-AES (inductively coupled plasma atomic emission spectrometer, ICPS-7510 Shimadzu, Tokyo, Japan). For kinetic study, samples were collected at fixed contact times, and analyzed (after filtration) for plotting the concentration decay curves. The sorption capacity (q_{eq}, mmol Sr g^{-1}) was determined by the mass balance equation:

$$q_{eq} = \frac{(C_0 - C_{eq}) \times V}{m} \quad (1)$$

For sorption isotherms, the sorbent dosage was set to 0.4 g L^{-1}, the initial concentration was varied between 10 and 600 mg Sr L^{-1} while the initial pH of the solution was fixed at pH 8.0. The suspension was stirred for 48 h. The pH was not controlled during the sorption but the final pH value was monitored together with the residual metal concentration. The experiments have been duplicated and the comparison of the duplicates appears as Run #1 and Run #2 in the Figures. The experimental conditions have been systematically checked regarding metal precipitation and sorption artifacts on experimental setup.

For desorption studies, the sorbents collected during the sorption kinetics were mixed with 0.5 M HCl solutions and samples were regularly collected and analyzed for evaluating the released Sr(II) and for plotting the desorption kinetics. For the study of sorbent recycling, the sorption and desorption procedures were used and a rinsing step was processed using demineralized water between each sorption and desorption step. The efficiency of sorption and desorption were compared for five successive cycles.

The presence of other metals may interfere with the removal of Sr (II). In order to evaluate the impact of alkali and alkali-earth elements (abundant in seawater and/or having similar physicochemical behavior in solution) on Sr(II) uptake, a series of experiments were performed with equimolar multi-component solutions (i.e., 1.3 mmol L^{-1}) at different pH values (in the range 3–8). The sorbent dosage was set at 0.125 g L^{-1}; the suspension was maintained under agitation for 48 h. After pH measurement and filtration, the residual concentrations were analyzed by ICP-AES and the sorption capacities were calculated by the mass-balance equation. The distribution ratio (L g^{-1}) was calculated by:

$$D = \frac{q_{eq}}{C_{eq}} \quad (2)$$

And the selectivity coefficient ($SC_{Me1/Me2}$) was deduced by:

$$SC_{Me1/Me2} = \frac{D_{Me1}}{D_{Me2}} = \frac{q_{eq,Me1} \times C_{eq,Me2}}{C_{eq,Me1} \times q_{eq,Me2}} \quad (3)$$

Sorption tests were also performed in fixed-bed columns. The sorbent was immobilized in a column (diameter: 5 mm; height: 47 mm). The ratio column diameter/particle size being much higher than 12, the wall effect can be neglected. The column was fed up flow (at flow rates: 0.2, 0.4 and 1 mL min^{-1}, corresponding to superficial flow velocities of 0.61, 1.22 and 3.06 m h^{-1}); 10 mL-samples were collected in series for analysis of outlet concentrations.

The models used for fitting uptake kinetics (i.e., pseudo-first order and pseudo-second order rate equations, PFORE and PSORE; and the Crank equation for resistance to intraparticle diffusion) and sorption isotherms (i.e., Langmuir, Freundlich and Sips equations) are summarized in Tables AM1 and AM2. Non-linear regression analysis was used for the determination of model parameters, while the determination coefficient was determined comparing experimental and simulated data (linear regression analysis). The Akeike information criterion was also applied for comparing the fits of experimental data with selected equations [53]. For the modeling of desorption kinetics (PFORE and PSORE, [54]) and breakthrough curves (Thomas equation [55]), the model equations are reported in the footnotes of relevant tables (see below).

2.5. Sr(II) recovery from seawater

Sorption tests on seawater samples were also performed in batch, using the same experimental procedure as with synthetic solutions: 500 mL of water (which pH was controlled to pH 4, 8 and 12, using either HCl or NaOH solutions) were mixed with 0.1 g of sorbent for 48 h (samples were collected at intermediary times for plotting kinetic curves). Semi-quantitative EDX analysis on loaded samples was used for determining the metals to investigate (i.e., Na(I), K(I), Mg(II), Ca(II), Sr (II), B(III), Ru(III) and Mo(VI)).

3. Results and discussion

3.1. Characterization of sorbents

In the preliminary part of the work, different formulations of bi-functionalized sorbents were compared to the sorption properties of mono-functionalized supports for selecting the best compromise (regarding Sr(II) uptake); results are summarized in the Section 3.2.1. Therefore, the characterization of the material was mainly focused on

this specific "optimized" sorbent (i.e., $PAO_{20}MMA_{80}/SiO_2$).

3.1.1. Morphology and textural properties

Sp herical silica-based resins have a p article size in the range 119–132 μm (Fig. AM1). The surface is coated by a polymer layer that gives to the sorbent an irregular surface topography. Fig. AM2 shows the BET analysis of raw SiO_2, $PMAA/SiO_2$ (mono-functionalized) and $PAO_{20}MAA_{80}/SiO_2$ (bi-functionalized) beads. While the chemical grafting of silica microparticles usually contributes to strongly decrease the specific surface area (SSA), the pore size and the pore volume [56], in the case of mono- and bi-functionalized silica beads, the textural properties shows contradictory trends. The SSA hardly changes with the successive modifications: f rom 69.1 $m^2 g^{-1}$ (SiO_2) t o 62.4 $m^2 g^{-1}$ ($PMAA/SiO_2$) and 64.7 $m^2 g^{-1}$ (bi-functionalized sorbent). Surprisingly, the post-modification (amidoxime grafting) slightly improves the SSA of the sorbent. However, the differences a re n ot m arked. The average pore size is of the same order of magnitude for the functionalized materials (around 300 Å) and little higher than the p ore size of raw silica beads (around 230 Å). The raw support can be considered a mesop orous silica based on the average size of the p ores (Fig. AM3). The coating of the silica beads with the polymer layers contribute to fill in the smallest p ores meaning that the average (global) p ore size slightly increases. Unexp ectedly, the p ore volume also increases with the p rogressive modification o f t he s up p ortf rom 0.299 c $m^3 g^{-1}$, to 0.376 $cm^3 g^{-1}$ for methacrylic acid-grafted silica, and up to 0.399 $cm^3 g^{-1}$ for the bi-functionalized material.

The average pore size largely exceeds the ionic radius of hydrated Sr (II) species (i.e., 1.26 Å [57]), meaning that the diffusion of strontium ions will not be strongly hindered by the p orous p rop erties of the composites.

3.1.2. Elem ental analysis

Table 1 reports the elemental analysis of different sorbents (homo- and heteropolymers supported on SiO_2: PAN, PMAA, PAO, at different ratios of substitution). The residue (to 100%, w/w) is p robably associated with SiO_2 core (the residue being Si element): the average value is 31.26% (with a standard deviation close to 0.85%), representing about 53.52 ± 1.45% (in weight fraction).

The comparison of the N content for PAO *vs.* PAN derivatives clearly demonstrates that the amidoximation of nitrile groups is quantitative (the N content is roughly doubled, consistently with expected reaction (Scheme 1b). The amidoximation is also quantitative for bi-functionalized materials: the N content (mmol N g^{-1}) is doubled while converting PAN_xMMA_{100-x}/SiO_2 into PAO_xMMA_{100-x}/SiO_2.

Table AM3 (a–d) shows the semi-quantitative EDX analysis of the surface of comp osite materials at different s tages o f t he s ynthesis of sorbents (also including after Sr(II) sorp tion). Obviously, these semi-quantitative analyses must be considered as an indication or a confirmation o f t he c hemical m odifications of th e ma terials al ong the synthesis procedure for the different compounds. In the SEM analysis, all materials keep the sp herical p rop erties of the silica p articles with surface coating due to grafting of the hydrocarbon chains. For mono-functional grafted composites, the trends are consistent with suggested synthesis routes. The amidoximation substantially increases the N atomic fraction (N_{AF}, almost doubled when converting PAN/SiO_2 to PAO/SiO_2: from 8.06 to 15.37%). The rate of substitution is close to 95%. This is associated with a relative increase of O atomic fraction due to the conversion of CN into $C(=NOH)NH_2$. On the other side, for $PMAA/SiO_2$, the grafting of acrylic acid allows drastically increasing O content (up to 55.52%); this is directly associated with the potential grafting of two oxygen atoms on carboxylic groups per monomer unit deposited on SiO_2 micro-particles. For bi-functional sorbents, using N_{AF} as the marker of substitution allows characterizing the quasi-linear increase in substitution rate ($AO_{Subst.Ratio}$) for PAN_xMAA_{100-x}/SiO_2 sorbents ($N_{AF} = 0.07 \times AO_{Subst.Ratio} + 1.49$) and PAO_xMAA_{100-x}/SiO_2 sorbents ($N_{AF} = 0.11 \times AO_{Subst.Ratio}$ R + 2.83). It is noteworthy that the comparison of N_{AF} for nitrilated intermediary materials and amidoximated sorbents demonstrates that the amidoximation rate varies between 83% and 91% for bi-functional materials. As expected, when the rate of amidoximation increases the atomic fraction of O decreases (from 50.5 and 52.9% to 30.8 and 40.2% for PAN_xMAA_{100-x}/SiO_2 and PAO_xMAA_{100-x}/SiO_2, respectively). The conversion of nitrilated mono-functional composite into amidoximated resin is almost quantitative (1.91 times the content of N in the PAN/SiO_2 material, close to the theoretical factor; i.e., 2). In the case of bi-functional composites, the comparison of PAN_xMAA_{100-x}/SiO_2 with PAO_xMAA_{100-x}/SiO_2 shows a lower degree of substitution (N_{AF} increases after amidoximation by a ratio lower than 1.81; (i.e., between 1.61 and 1.81)). The presence of metacrylic acid moieties limits the efficiency of the amidoximation step. This can be explained by two main reasons: (a) the limitations due to steric hindrance, and/or (b) the inhibiting effect associated with the presence of polar carboxylic groups.

3.1.3. Thermal degradation

Fig. AM4 shows the thermogravimetric analysis of $PAN_{20}MAA_{80}/SiO_2$ and its amidoximated derivative (i.e., $PAO_{20}MAA_{80}/SiO_2$). The comparison of TGA profiles shows relatively close behaviors. Below 269.1–266.5 °C, superficial water is released from the materials with a weight loss limited to 1.41% and 2.78% for $PAN_{20}MAA_{80}/SiO_2$ and $PAO_{20}MAA_{80}/SiO_2$, respectively. A second weight loss step (representing 5.55% and 8.26% for the nitrile and amidoximated materials, respectively) is observed between 269.1–266.5 °C and 564.9–493.7 °C. This weight loss may be associated with the degradation of polyacrylonitrile [58,59], amidoxime substituents [60], poly methacrylic acid compound [61], and to the depolymerization of the silica coating. The amidoximation decreases the stability of the composite (highest weight loss and lower temperature of degradation) [60]. Actually, this second step combines different degradation mechanisms associated with the diversity of polymer and functional groups that coat silica particles: several weak shoulders/waves are observed, especially on the TGA profile of nitrile-composite (this is less apparent for amidoximated material). The third step in the thermal degradation corresponds to the degradation of the char, above 493.7 °C for $PAO_{20}MAA_{80}/SiO_2$ and above 564.86 °C for $PAN_{20}MAA_{80}/SiO_2$; the total weight losses correspond to 13.63% and 7.63%, respectively. This means that the polymer layer coating silica beads is relatively limited: less than 8% in the case of the intermediary compound (nitrile-composite) and less than 14% for the amidoximated bi-functionalized composite.

Fig. AM5 compares the DTG (derivative thermogravimetry) profiles for the thermal degradation of the two composites. The nitrile-composite shows a smoothed (poorly resolved) curve with a very broad exothermic band (in the range 100–400 °C) without any specific peak. On the opposite hand, after amidoximation the DTG curve shows a little shorter range of temperature (in the range 100–394 °C) for the poorly resolved exothermic band, which is completed by twin peaks at 265.14 °C and 272.55 °C; another small exothermic peak is also detected at 586.48 °C. The cyclization of nitrile was reported at 584 °C [62]. In the case of silica/PAN hollow nanoparticles and silica/poly

Table 1
Elemental analysis of materials (C, N, H and O elements, wt% and mmol N g^{-1}).

Materials	C (%)	N (%)	N (mmol g^{-1})	H (%)	O (%)
PAN	21.4	6.9	4.93	3.6	36.28
PAO	22.02	14.18	10.12	4.1	29.2
PMAA	21.8	0.2	0.14	4.62	40.08
$PAN_{20}MAA_{80}/SiO_2$	17.6	2.18	1.56	3.71	46.31
$PAN_{50}MAA_{50}/SiO_2$	15.2	4.57	3.26	3.8	45.33
$PAN_{80}MAA_{20}/SiO_2$	13.2	5.65	4.03	3.86	45.89
$PAO_{20}MAA_{80}/SiO_2$	17.9	4.71	3.36	5.01	41.18
$PAO_{50}MAA_{50}/SiO_2$	15.8	9.82	7.01	5.13	38.35
$PAO_{80}MAA_{20}/SiO_2$	14.3	10.93	7.80	5.21	38.66

acrylic acid hollow nanogels, the maximum exotherm peak was observed close to 440 °C for the two composites (indifferently of the grafted polymer) [63].

3.1.4. FTIR analysis

FTIR spectroscopy was used for characterizing SiO_2, PAN/SiO_2 (Fig. AM6a), $PMAA/SiO_2$ (Fig. AM6b), PAN_xMAA_{100-x}/SiO_2, and PAO_xMAA_{100-x}/SiO_2 (at different copolymerr atios (Fig. AM7a,b,c)). The spectra were also characterized for $PAO_{20}MAA_{80}/SiO_2$ after Sr(II) sorption, after metal desorption and after five cycles of sorption desorption. Tables AM4–AM7 report the main characteristics peaks (wavenumbers) and their assignments.

Raw silica shows peaks at 1110 cm^{-1}, 806 cm^{-1}, and 474 cm^{-1}, which are assigned to asymmetric stretching and bending vibrations of Si—O—Si bonds [64–66]. The first two peaks are overlapped with C—N and C—C respectively in polymer-coated SiO_2 [64,67,68]. The broad peaks at 3442 cm^{-1} and 1632 cm^{-1} are assigned to OH groups in SiO_2, associated with water binding at the surface of the solid [65].

After acrylonitrile grafting (in both homo- and hetero-polymer), some specific peaks appear including nitrile groups 2280–2240 cm^{-1} [69,70]. Carboxylate groups associated to the incorporation of MAA (both in homo- and hetero-polymers) are identified at 1750–1725 cm^{-1} [70–72]. Other peaks attributed to carboxylate ester groups are also identified at 1420–1300 cm^{-1} for O—C=O group stretching vibrations, which overlapped with C-N stretching of amide and —OH bending of amidoxime groups in copolymeric sorbents [70,73]. These peaks may overlap with those of silicate and eventually with amide groups of amidoxime [74] (occurring at the second step of the modification in the co-polymer grafting). After the conversion of nitrile to amidoxime, the peak at 2280–2240 cm^{-1} fully disappears, showing the effective and complete amidoximation; this is consistent with the conclusions raised from elemental analysis. In addition, the intensity of the broad peak at around 1600–1690 cm^{-1} increases due to the grafting of the amide groups of amidoxime [75]. The peak at 1050–990 cm^{-1} is attributed to N—O stretching band [66]. In some cases (especially for SiO_2 composites), this band may overlap with the broad band of Si—O—Si and/or with C—N band that appears at 1090–1020 cm^{-1} [66].

The sorption of Sr(II) is characterized by some shifts or broadening of bands. For example, the broad band around 3400–3600 cm^{-1} tends to enlarge after metal binding; this is probably associated with the interaction of strontium cation with nitrogen and hydroxyl groups (direct and/or changes in their chemical environment). In the case of mono-functionalized $PMAA/SiO_2$, the most significant changes are observed in the range 1500–1700 cm^{-1} with the decrease in the intensities of the peaks at 1635 cm^{-1} and 1680 cm^{-1}, replaced by a peak at 1641 cm^{-1}. This is directly associated with the interaction of Sr(II) with carboxylate groups. For PAO/SiO_2, the intensities of the band at 943 cm^{-1} (N—O stretching) and the shoulder at 569 cm^{-1} (assigned to —OH and C—H bending vibrations) decrease with metal binding. This may be explained by the interaction of Sr(II) with amidoxime moiety. The low sorption capacities obtained with mono-functionalized sorbents (see below) may explain the difficulty to identify large changes in the FTIR spectra. Bi-functionalized sorbents (especially for $PAO_{20}MAA_{80}/SiO_2$) have higher affinity for Sr(II); therefore, the spectra are also more influenced by the sorption of the metal ions. More specifically, the most representative modifications are reported at:

(a) 2426 cm^{-1} and satellite peaks around 2360 cm^{-1}: new small peaks, which could be associated with carbon dioxide at the surface of the sorbent.
(b) 1763 cm^{-1} peak was shifted to 1718 cm^{-1}; associated with carboxylic groups (C = O stretching) for $PAO_{20}MAA_{80}/SiO_2$ (not detectable for other PAO_xMAA_{100-x}/SiO_2 sorbents that have much lower acrylic acid fractions).
(c) 1360–1430 cm^{-1}: peak widening; the sharp peak at 1383 cm^{-1} (C-N stretching and OH bending) is replaced with a broad band of increasing widening when the fraction of amidoxime decreases; in addition, a peak at 1398 cm^{-1} and two shoulders at 1429 cm^{-1} and 1358 cm^{-1}) also appear after functionalization.
(d) 825 cm^{-1}: new sharp peak appearing only for bi-functionalized materials (sometimes associated with nitrate compounds [70]).

The changes in the FTIR spectra after Sr(II) sorption confirm the simultaneous contributions of carboxylic groups (from MAA), amine and hydroxyl groups (from amidoxime moiety) in the binding of strontium.

3.1.5. XPS analysis

The XPS survey spectra for $PAN_{20}MAA_{80}/SiO_2$, $PAO_{20}MAA_{80}/SiO_2$ and $PAO_{20}MAA_{80}/SiO_2$ + Sr are reported on Fig. 1. The XPS spectra confirm the presence of silica core (Si *2*p and Si *2s*), and polymer markers (C *1s*, N *1s* and O *1s*). The sorption of Sr(II) is confirmed by the appearance of the typical peaks of Sr element (Sr *4*p, Sr *3*d, Sr *3*p and Sr *3s*).

Table AM8 shows the high resolution spectra (HRES) of the C *1s*, O *1s*, N *1s* and Si *2*p signals. Table AM9 reports the HRES of Sr *3*d, Sr *4*p, Sr *3*p and Sr *3s* for $PAO_{20}MAA_80/SiO_2$ after metal sorption. These tables summarize the assignments, atomic fractions and full-width at half maximum (FWHM) for the deconvolution of the different signals. These analyses contribute to confirm the successful chemical modification of

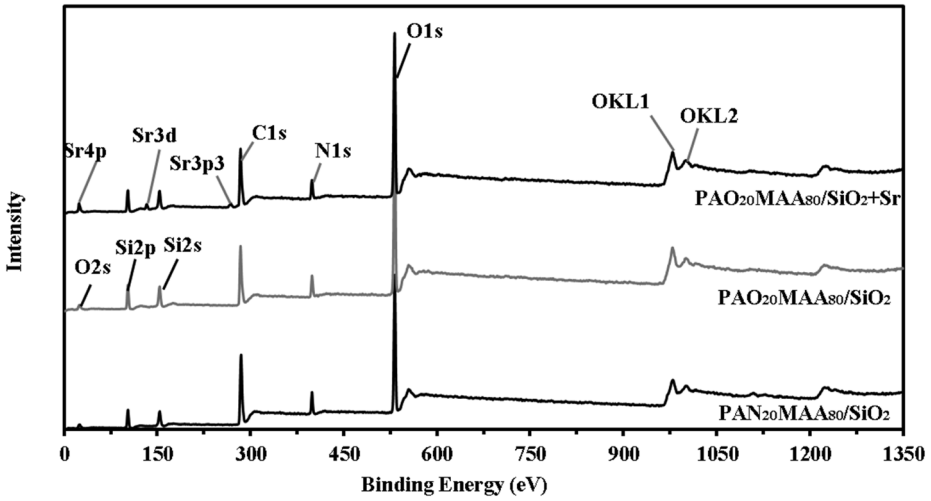

Fig. 1. XPS analysis (survey) of functionalized materials ($PAN_{20}MMA_{80}/SiO_2$, $PAO_{20}MMA_{80}/SiO_2$ = sorbent, sorbent + Sr(II)).

the support and the interpretation of binding mechanisms.

The composition of the composite bi-functionalized materials offers a wide diversity of signals associated to the different bonds and chemical environments of the C, O and N elements in the different polymer-coated sorbents. For C *1s* signal, the deconvolution of the signal shows the presence of many different bonds, associated with methacrylic, acrylonitrile and/or amidoxime moieties: C—C and C—H (or adventitious C) around 284.3 ± 0.3 eV; C—O or C═N at 286.2 ± 0.4 eV [76]; O—C═O (carboxylic groups) at 287.3 ± 0.2 eV; C≡N at 288.0 ± 0.2 eV [77–80]. The composite materials (supported on SiO_2) contain MAA with either nitrile or amidoxime ending groups; this is confirmed by the disappearance of C≡N signal (at 288.13 eV) when $PAN_{20}MAA_{80}/SiO_2$ is amidoximated (together with the appearance of a band corresponding to C═NOH, at 286.2 eV). The sorption of Sr(II) involves a small decrease in the binding energies but also an increase in the atomic fractions of some C *1s* bands, including both C (carboxyl) and C (amidoxime) groups (from 10.26 to 12.6% and from 6.13 to 17.97%, respectively).

The chemical modification of the $PAN_{20}MAA_{80}/SiO_2$ is also characterized by the changes observed on N *1s* signal. Ma et al. [76] reported the presence of two bands for N *1s* on polyacrylonitrile fibers at 398.63 eV and 400.60 eV (nitrile group, C≡N, and shake-up line, respectively). After amidoximation, the N *1s* bands appeared at 398.37 eV (C═N—O, part of amidoxime) and at 398.82 eV (C-NH_2). Li et al. [81] investigated the sorption of uranium on MOF functionalized with amidoxime groups and reported three bands at 399.2 eV, 400.4 eV, and 401.45 eV for C-NH_2 or C═N, C—NOH and C-NH_2^+, respectively. This is consistent with the groups identified on reduced graphene oxide grafted with amidoxime groups [82]. With $PAO_{20}MAA_{80}/SiO_2$, the two peaks corresponding to N═C—OH and NH_2 are detected at around 398.9 eV and 400.65 eV, respectively; the differences in BEs are not very marked compared with the nitrile and shake-up lines of precursor. After strontium binding, the BEs of the signals are weakly shifted by 0.15 eV toward higher BE for N═C—OH (proving the donation of lone pair of electrons from N through the coordination of Sr(II) with N [83]) and lower energy for NH_2. Wang et al. [78] investigated uranyl sorption on hydrolyzed amidoximated-PAN fibers and observed that the signal corresponding to $-NH_2$ was slightly shifted after U(VI) binding; while —NOH bond did not appear to be affected by metal binding and a new peak assigned to N-U complexation (around BE = 404.68 eV) appeared. Here also, consistently with Wang et al. [78], a new weak band appears at 405.3 eV, which is associated with the direct interaction of the metal with N (from amino groups).

For O *1s*, Wang et al. [78] identified three peaks, on amidoximated-PAN fibers, at 531.18 eV, 530.34 eV and 529.54 eV corresponding to —OH, —NO and —CO groups, respectively. For amidoximated —MOF, Li et al. [81] showed substantially higher binding energies for —OH, C═O and C—O groups at 531.4 eV, 532.1 eV and 532.9 eV, respectively. Chen et al. [82] synthesized amidoxime-functionalized reduced graphene oxide and they assigned the bands at 531.48 eV, 532.60 eV and 533.70 eV to $-COO^-$, >C═O and —C—OH groups, respectively. In the composite sorbents, the presence of SiO_2 core introduces a complementary band at around 532.1 ± 0.2 eV. For $PAN_{20}MAA_{80}/SiO_2$, O element only appears in the silica compartment (532.27 eV; atomic fraction, AF, close to 95%) and in the methacrylic acid (530.65 eV); however, traces of O-Na bond are also identified at 529.04 eV (residue from synthesis procedure). After amidoximation, the fraction of O associated with SiO_2 core decreases due to the appearance of $-C(NH_2)$═N—OH moieties (from 95 to 92%), not compensated by the fraction of C═NOH that appeared, but by the increasing proportion of C═O. This may be explained by the conversion of some nitrile groups to carboxylic acid groups by the effect of temperature (and activation technique) and reagents (pH, alkaline conditions) [84]. The sorption of Sr(II) is followed by the appearance of a new peak at BE = 528.2 eV (weak signal) and the relative increase in the AF of –C═O. This means that Sr(II) binding may involve some carboxylic groups as mono-dentate ligand and/or combined with amine groups to form multi-dentate complex.

The sorption of Sr(II) is confirmed on the survey spectrum by signals at binding energies close to 18.42 eV (Sr *4*p), 134 eV (Sr *3*d) and 277 eV (Sr *3*p). The deconvolution of Sr *3*d HRES spectrum shows the presence of 2 doublet-peaks (spin-orbital components, corresponding to the Sr $3d_{5/2}$ and Sr $3d_{3/2}$ spin-orbital splits) for two Sr chemical environments. The Sr-O bond is the most intense (largest atomic fraction), which is associated with Sr $3d_{5/2}$ at 132.48 eV and Sr $3d_{3/2}$ at 134.09 eV. Gregurec et al. [85] reported the Sr $3d_{5/2}$ at BE close to 133.5 eV in the case of strontium binding by carboxylic groups of poly(acrylic) brushes. Similarly, Wang et al. [27] confirmed the binding of Sr(II) on carboxylic groups of methylacrylic acid/silica composite by the presence of two peaks at 133.55 eV (Sr $3d_{5/2}$) and 135.09 eV (Sr $3d_{3/2}$). In the case of algal/PEI beads functionalized with amidoxime groups, Wei et al. [41] reported Sr(II) sorption on amidoxime reactive groups with Sr $3d_{5/2}$ and Sr $3d_{3/2}$ bands at lower BEs (i.e., 132.91 eV and 134.59 eV, respectively). The coexistence of the four peaks (with very low AF for the peaks at 133.87 and 135.55 eV) means that amidoxime groups constitute the most active binding groups although carboxylate groups contribute marginally for strontium chelation or stabilization. Other

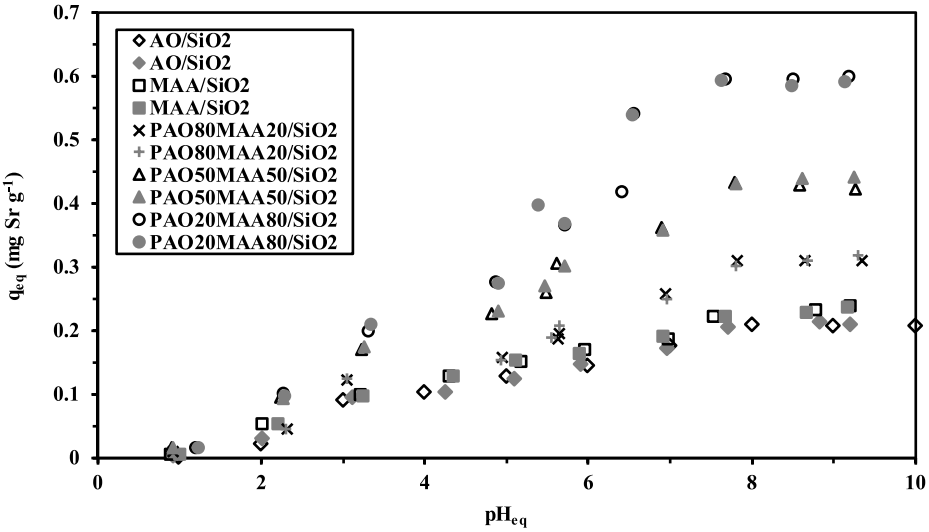

Fig. 2. Effect of pH on Sr(II) sorption using mono-functional and bi-functional polymers coated silica microbeads (Sorbent dosage, SD: 0.4 g L^{-1}; C_0: 50 mg L^{-1} = 0.59 mmol Sr L^{-1}; agitation time: 48 h; agitation speed, 170 rpm; T: 22 ± 2 °C; duplicated experiments: Run #1:opened symbols, Run #2: closed symbols).

signals for Sr are observed: Sr *4*p (at 18.42 eV), Sr *3*s (poorly resolved peak, at 355.69 eV), and Sr *3*p (two different spin-orbital splits: Sr $3p_{3/2}$ at 268.3 eV, and Sr $3p_{1/2}$ at 278.65 eV). These observations confirm the multi-binding groups of Sr(II) onto the sorbent through two different types of bonds involving probably amine and carboxylate groups from amidoxime and acrylic moieties, respectively, and hydroxyl groups from amidoxime and/or acrylic moieties.

3.1.6. Titration – pH_{PZC}

The pH_{PZC} of the optimized bi-functionalized sorbent is determined by the pH-drift method (Fig. AM8). The average value is close to 6.47 (±0.02), showing the limiting effect of the concentration of the background salt (0.1 M *vs.* 1 M NaCl solution). The co-existence of methacrylic and amidoxime groups brings reactive groups with specific proton exchange properties. For example, the pK_a values of amidoxime-based compounds strongly depend on the substituents but ranges between 3 and 5.3 in most cases [86]. The pK_a of methacrylic acid is reported close to 4.65 [87]; the polymerization and the chemical modification of polymethacrylic chain strongly modulate the acid-base properties of functionalized material [88].

Selected functionalized sorbent (i.e., $PAO_{20}MMA_{80}/SiO_2$) is protonated in acidic solutions; meaning that the sorbent can electrostatically attract anionic species at pH lower than 6, and repulse cationic species in acidic conditions (pH lower than 3–4). This protonation also opens possibilities for ion-exchange mechanisms at intermediary acidic pH values (moderate pH around pH 5) and metal complexation at neutral pH.

3.2. Sorption studies

3.2.1. Effect of pH and sorbent selection

Fig. 2 reports the comparison of Sr(II) sorption capacities for mono- and bi-functionalized silica composites (including variable levels of amidoxime grafting). The experimental series were duplicated and the overlapping of the curves clearly demonstrates the reproducibility of sorption performances. At pH 1, the sorption properties for strontium are negligible for the different materials. The strong protonation of reactive groups limits the capacity of the sorbent to bind strontium, which is present as Sr^{2+} (about 84.7%) and $SrNO_3^+$ (15.3%). The acid used for pH control leads to the presence of nitrate anions that may bind to protonated reactive groups; the negligible sorption capacity means that Sr(II) could not be sorbed as ion pair at the surface of the sorbent. When the pH increases, the sorption capacity linearly increases up to pH 7.5–8. The competition of protons decreases and the support progressively deprotonates making possible the binding of strontium cations. Sr(II) is present as free strontium species at pH above 4 (with progressive decrease of the fraction of strontium nitrate cation). Above pH 8, the sorption stabilizes; similar observations were reported by Asgari et al. [37] for Sr(II) sorption on MOF. It is noteworthy that the pH-profiles overlap for mono-functional silica beads (both AO and MAA modified beads, with sorption capacity below 0.24 mmol Sr g^{-1} (under selected experimental conditions). The substitution of AO on MAA/SiO_2 backbone (i.e., bi-functional sorbents) increases the sorption of Sr(II) (compared with mono-functional beads). This increase depends on the yield of substitution; actually, highest sorption is obtained at the lowest (tested) rate of substitution (i.e., 20/80 ratio between AO and MAA moieties). The maximum sorption capacities stabilize around 0.31 mmol Sr g^{-1} for $PAO_{80}MAA_{20}/SiO_2$, 0.44 mmol Sr g^{-1} for $PAO_{50}MAA_{50}/SiO_2$, and up to 0.59 mmol Sr g^{-1} for $PAO_{20}MAA_{80}/SiO_2$. Fig. AM9 shows the correlation between the rate of AO substitution and the maximum sorption capacity (obtained on the stabilization plateau reached above pH 7.5).

Table AM3 (a-d) compares the semi-quantitative EDX surface analysis of the different sorbents after Sr(II) sorption. This data confirm the observations from Fig. 2: the sorption of Sr(II) decreases with the excessive amidoximation of intermediary PAN_xMAA_{100-x}/SiO_2 composite. However, compared with $PMAA/SiO_2$, the presence of amidoxime groups increases the binding of Sr(II): Sr_{AF} increases from 1.59 (for $PMAA/SiO_2$) to 2.19 (for $PAO_{20}MAA_{80}/SiO_2$), while a larger substitution rate decreases metal uptake. These observations are consistent with Fig. AM9.

Figure AM10 shows the $\log_{10}$-plots of the distribution ratio ($D = q_{eq}/C_{eq}$, L g^{-1}) *vs* pH_{eq}. The insert focuses on the linear section of these curves (registered between pH 2 and 8). The slopes vary between 0.109 and 0.176. In ion-exchange reactions, the slope is frequently associated with the stoichiometric ratio for proton exchange at the surface of the sorbent and metal ions. In present cases, the slope analysis cannot be correlated to appropriate ion-exchange ratio.

The pH frequently changes during the sorption process and it is important correlating sorption properties with these pH variations. In the case of mono- and bi-functionalized silica sorbents, the pH variation is relatively limited (by less than 0.5 pH unit) (Fig. AM11): the pH slightly increases at pH 4 and 5 and tends to slightly decreases at pH above 6. This is consistent with the study of pH_{PZC} (around 6.5, for $PAO_{20}MAA_{80}/SiO_2$), although the pH variations are much less marked in the presence of strontium.

Based on these results, further experiments are performed at pH_0 8 (corresponding to pH_{eq} around 7.4–7.6). The optimum sorption being obtained with the lowest rate of AO substitution, further experiments are also carried out with this specific optimized sorbent (i.e., $PAO_{20}MAA_{80}/SiO_2$). Alexandratos et al. [46] discussed the interest of bi-functionalization of polyacrylonitrile fibers (using amidoxime and amine groups) for improving the sorption of U(VI). They recognized several effects for this double functionalization: (a) the amine groups (preferentially diethylenetriamine, DETA) introduce additional sorption sites for U(VI) binding, and (b) the interaction of DETA with AO (though hydrogen bonding) contributes to improve the dissociation of the acidic N—O—H group. In the case of bi-functional (carbonyl and phosphoryl groups) resins, Alexandratos and Smith reported the counter-current effects of the bi-functionalization through intraligand cooperation and intraligand hydrogen bonding mechanisms. In the case of uranyl sorption (as carbonate anionic species), the synergistic effect of positive charge and amidoxime coordination have been demonstrated to explain the high efficiency of bi-functional resins [47]. Piechowicz et al. [39] explained the remarkable sorption of uranyl from seawater onto a bi-functional polymer by the simultaneous weak coordination of uranyl with chelating carboxylates and monodentate binding by amidoxime groups. Bi-functionalization (amidoxime and sulfur compounds) was also discussed by Qu et al. [48] for improving the selective removal of Hg(II) from multi-component solutions. The literature is much less abundant concerning the enhancement of Sr(II) sorption properties using bi-functionalized sorbents. El-Naggar et al. [89] described the enhancement of sorption properties for divalent cations (including Sr(II)) while modifying a resin by simultaneously grafting different reactive groups (P-based ligands). The multi-group cooperation, called supported ligand synergistic interaction, depends on the target metal and the acidity of the solution. Recently, Younis et al. [43] reported a substantial increase in Sr(II) (and Ca(II)) sorption by simultaneous grafting of sulfonic and carboxylic groups on a polymer backbone (styrene butadiene/acrylonitrile resin) for metal recovery from highly saline oilfield wastewater.

3.2.2. Uptake kinetics

The uptake kinetics can be controlled by the resistance to bulk diffusion, to film diffusion and to intraparticle diffusion, in addition to the proper reaction rate of sorption. Providing a sufficient agitation to prevent particle settling and heterogeneous distribution of the solute in the solution and to minimize the resistance to film diffusion allows neglecting the first two diffusion criteria. For film diffusion, the resistance to mass transfer is usually limited to the first minutes of contact. Therefore, the resistance to intraparticle diffusion (RIDE, the so-called Crank equation) is more appropriate for the modeling of kinetic

profiles on a wider time range (Table AM1, see Additional Material Section). The sorption process can be modeled using, by analogy with homogeneous reactions, the pseudo-first order rate equation (PFORE) and/or the pseudo-second order rate equation (PSORE) (Table AM1). Fig. 3 compares the fits of experimental data for Sr(II) uptake at three different initial metal concentrations using $PAO_{20}MAA_{80}/SiO_2$ and the three models. The solid lines correspond to fitted curves with the parameters summarized in Table 2. Fig. AM12 shows an example of reproducibility test for uptake kinetics. The sorption of Sr(II) is relatively fast: 25–60 min of contact are necessary for reaching equilibrium, depending on metal concentration. More than 90% of total sorption occurs within the first 25 min of contact. The small size of the sorbent (around 125 μm), the large pore size of the composites and the thin polymer layers (which controlled the diffusion thickness to be passed through) may explain the relatively fast sorption kinetics. The hydrated ionic size of strontium is close to 1.26 Å [57]; this means two orders of magnitude lower than the average pore size of the sorbent.

The superimposition of the curves with the three models shows the difficulty to discriminate between the different models, at least at higher metal concentrations. The curve obtained at the lowest Sr(II) concentration (i.e., C_0: 0.604 mmol Sr L^{-1}) shows a greater inaccuracy in the time range 15–30 min (corresponding to the highest curvature). In this case, the best fit was obtained with the PFORE; this is confirmed by both the determination coefficient (i.e., R^2) and the value of the sorption capacity at equilibrium ($q_{eq,1}$, calculated value from PFORE) closer to the experimental value ($q_{eq,exp}$) than $q_{eq,2}$ (calculated from PSORE). The PFORE is frequently associated with physical sorption while the PSORE counts on chemical interactions. The indistinct fitting trends cannot help in discriminating between the two types of interaction modes. The complementary analysis of fitting parameters with the Akaike information criterion (AIC) shows that at low metal concentration the curve is better fitted by the PFORE while at higher concentration the RIDE better simulates the kinetic profiles. The values of apparent rate coefficients (k_1 and k_2) slightly vary with metal concentration: in the range 8.9–16.7 × 10^{-2} min^{-1} for PFORE and between 19.3 and 12.2 × 10^{-2} L $mmol^{-1}$ min^{-1} for PSORE. At higher concentrations (i.e., 2.37 and 3.57 mmol Sr g^{-1}), the RIDE fits well the kinetic profiles. The effective diffusivity coefficient (D_{eff}) varies between 6.8 × 10^{-11} m^2 min^{-1} and 11.7 × 10^{-11} m^2 min^{-1}; These values are about three orders of magnitude lower than the self-diffusivity of Sr(II) in water (i.e., 4.75 × 10^{-8} m^2 min^{-1}, [90]). This is a confirmation that the resistance to intraparticle diffusion plays a role in the control of the uptake kinetics. These values are about one order of magnitude lower than the values reported for diffusivity of Sr(II) in sorbent based on titanium phosphate (i.e., 6 × 10^{-10} m^2 min^{-1}) [91] but several orders of magnitude higher than the effective diffusivity of Sr(II) into straw-derived char (5.4 × 10^{-14} m^2 min^{-1}) [92]. For macroporous resin, Sr(II) diffusivity was evaluated close to 1.2 × 10^{-8} m^2 min^{-1} [93]. In the case of Dowex resins, Boyd and Soldano [94] identified the contribution of crosslinking ratio to the control of diffusion properties (in the range: 1.37–2.03 × 10^{-9} m^2 min^{-1}); similar value was reported for Dowex 50 W-X8 resin (i.e., 1.17 × 10^{-9} m^2 min^{-1}) [95]. These different data confirm that the mass transfer properties of the bi-functionalized SiO_2 composite are roughly comparable to those reported for conventional resins.

3.2.3. Sorption isotherms

The distribution of the solute between the liquid and solid phase for increasing concentrations is described by sorption isotherms. The sorption isotherms can be fitted by different models such as Langmuir equation (mechanistic model) and Freundlich or Sips equations (empirical models). Fig. 4 compares the modeling of Sr(II) sorption isotherm at pH_0 8 for $PAO_{20}MAA_{80}/SiO_2$ sorbent. The superimposition of the two duplicated series confirm the reproducibility of sorption performance on selected sorbent. The general shape of the curve is characterized by a progressive increase of sorption capacity followed by an asymptotic plateau (for equilibrium concentration above 4 mmol Sr g^{-1}). This asymptotic trend is not consistent with the power-type function represented by the Freundlich equation: this is consistent with Table 3 that summarizes the fitted parameters. The initial slope of the curve is representative of the affinity of $PAO_{20}MAA_{80}/SiO_2$ for Sr(II). Actually, this initial slope is not steep; showing that appreciable sorption capacities require high metal concentration: the removal of Sr(II) traces will require high sorbent dosage for achieving complete metal recovery. The initial slope corresponds to the coefficient $q_{m,L} \times b_L$ (L g^{-1}); in the present case, this term, analogous of distribution ratio, tends to 2.14 and 2.29 L g^{-1} for series #1 and #2, respectively. The comparison of the fits with experimental data show that the Freundlich and the Sips equations tend to overestimate the sorption capacities at the saturation of the sorbent, contrary to the Langmuir equation. The insert shows the initial section of the curve where the Langmuir equation underestimates sorption capacities while the Freundlich underestimates experimental data; the Sips equation fits better the profile

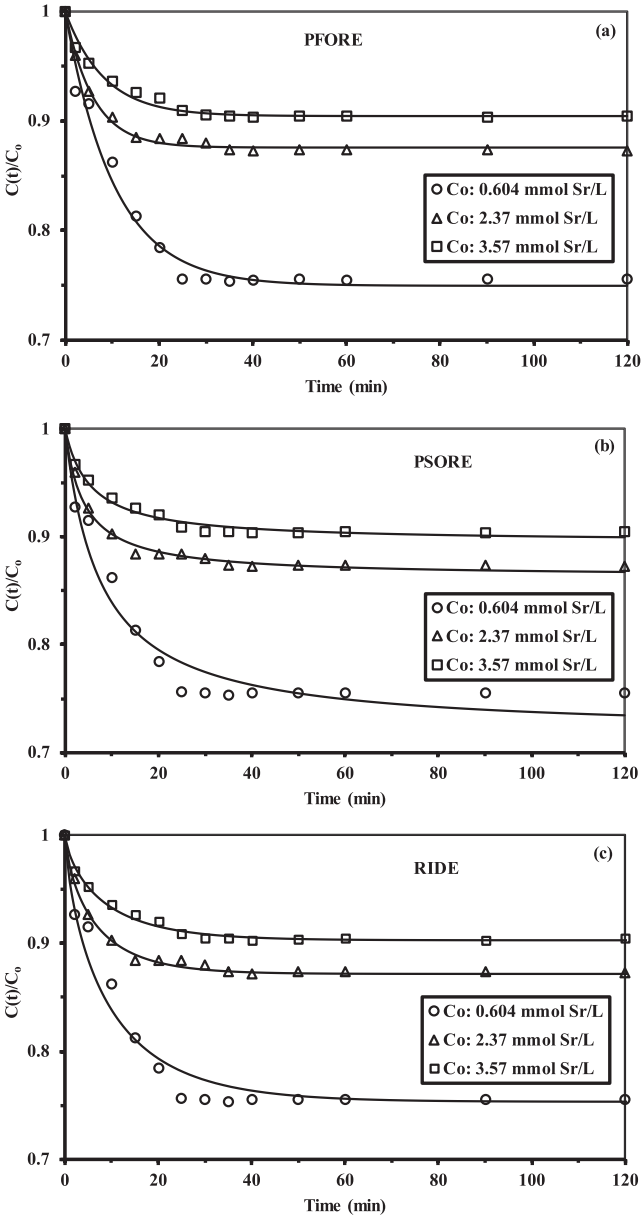

Fig. 3. Sr(II) uptake kinetics using $PAO_{20}MAA_{80}/SiO_2$ for different initial concentrations – Modeling with the PFORE(a), the PSORE (b) and the RIDE (c) (pH_0: 8; pH_{eq}: 7.59–7.51; SD: 0.25 g L^{-1}; agitation speed: 170 rpm; T: 22 ± 2 °C).

Table 2
Parameters of kinetic models for Sr(II) sorption using $PAO_{20}MAA_{80}/SiO_2$.

		C_0 (mmol Sr L^{-1})			
		0.6		2.37	3.57
Model	Parameter	Run #1	Run #2		
Experimental	q_{eq} (mmol U g^{-1})	0.591	0.592	1.21	1.36
PFORE	$q_{eq,1}$ (mmol U g^{-1})	0.608	0.604	1.18	1.36
	$k_1 \times 10^2$ (min^{-1})	8.88	9.59	16.7	12.1
	R^2	0.982	0.981	0.993	0.979
	AIC*	−127.6	−132.3	−159.6	−157.8
PSORE	$q_{eq,2}$ (mmol U g^{-1})	0.703	0.683	1.30	1.50
	$k_2 \times 10^2$ (L $mmol^{-1}$ min^{-1})	15.5	19.3	18.9	12.2
	R^2	0.947	0.958	0.992	0.983
	AIC*	−110.4	−114.4	−154.3	−156.2
RIDE	$D_e \times 10^{11}$ (m^2 min^{-1})	6.79	7.30	11.69	9.30
	R^2	0.958	0.971	0.996	0.991
	AIC*	−119.5	−123.0	−167.2	−164.8

AIC (calculated on C(t)/C_0 values). D_0 (strontium): 4.75 × 10^{-8} m^2 min^{-1}.

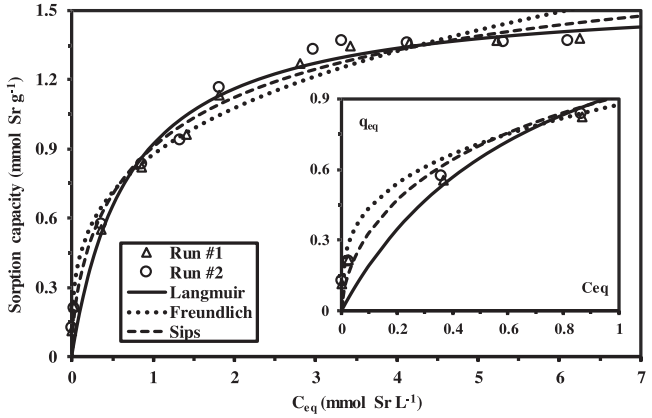

Fig. 4. Sr(II) sorption isotherm using $PAO_{20}MAA_{80}/SiO_2$ – Modeling with Langmuir, Freundlich and Sips equations (C_0: 4–600 mg Sr L^{-1} = 7.71–7.49; SD: 0.4 g L^{-1}; agitation time: 48 h; agitation speed: 170 rpm; T: 22 ± 2 °C).

Table 3
Parameters of models for Sr(II) sorption isotherms using $PAO_{20}MAA_{80}/SiO_2$.

Model	Parameter	Run #1	Run #2	Combined
Experimental	q_m (mmol U g^{-1})	1.379	1.371	1.379
Langmuir	$q_{m,L}$ (mmol U g^{-1})	1.575	1.573	1.574
	b_L (L $mmol^{-1}$)	1.356	1.454	1.405
	R^2	0.990	0.983	0.988
	AIC	−53.6	−50.3	−53.4
Freundlich	k_F	0.869	0.881	0.875
	n_F	3.349	3.361	0.875
	R^2	0.971	0.959	0.968
	AIC	−50.9	−47.0	−50.8
Sips	$q_{m,S}$ (mmol U g^{-1})	1.981	2.060	2.021
	b_S (L $mmol^{-1}$)	0.829	0.807	0.817
	n_S	1.556	1.675	1.617
	R^2	0.988	0.977	0.984
	AIC	−53.0	−48.0	−52.8

AIC (calculated on q_{eq} values).

at low residual metal concentration. Table 3 confirms that the Langmuir equation fits slightly better experimental curve than the alternative models. However, the calculated sorption capacity at saturation of the monolayer (i.e., $q_{m,L}$) significantly overestimates the maximum sorption capacity: 1.57 mmol Sr g^{-1} *vs.* 1.38 mmol Sr g^{-1}. The affinity coefficient (i.e., b_L) stands around 1.41 L $mmol^{-1}$. The AIC calculation normalizes the fitting of experimental data for the different models in function of the number of adjustable parameters. The Sips model that includes a third-adjustable parameter (compared with the two other models) could improve the quality of the fit; this is not the case, as shown by both the determination coefficients and the AIC values.

Table 4
Comparison of Sr(II) sorption properties of $PAO_{20}MAA_{80}/SiO_2$ with alternative sorbents (optimum pH, equilibrium time, Langmuir parameters).

Sorbent	pH	Time	$q_{m,L}$	b_L	Ref.
Clay	3	300	0.034	294	[99]
Almond green hull	6	3	1.33	0.421	[100]
Oxidized multiwall carbon nanotubes	7	1440	0.076	53.3	[10]
Moss	6	240	0.149	5	[16]
Magnetic chitosan beads	8.2	360	0.132	–	[101]
Zr-Sb oxide/PAN composite	4.74	270	0.498	73.6	[102]
Mixed Ni-K ferrocyanide/hydrated TiO_2	7.8	180	1.598	0.366	[31]
Co-aminophosphonic chitosan	6	60	0.0389	78.0	[103]
Saccharomyces cerevisiae	3–4	2000	0.427	3.08	[14]
Nd-BTC-MOF	8	60–90	0.667	0.876	[37]
Melamine-styrene resin	8	240	1.63	3.33	[104]
Magnetic zeolite nanocomposite	6	20–30	1.01	1.31	[5]
T-46 (sulfonic)/A-33 (quaternary) mixed resins	7	30	0.109	8.39	[105]
Graphene oxide	6	1440	1.573	0.876	[106]
Amidoximated algal/PEI beads	6	60–90	2.36	2.01	[107]
Carboxyl-functionalized SiO_2	10	30	0.913	1822	[27]
Zeolite	7.9	10	0.272	10.9	[108]
CHA-type zeolite	7	60	0.132	–	[109]
$PAO_{20}MAA_{80}/SiO_2$	8	40–60	1.57	1.41	This work

Time: min; $q_{m,L}$: mmol Sr L^{-1}; b_L: L $mmol^{-1}$.

Table 4 compares the sorption properties of selected composite with alternative sorbents reported in literature. Combining the kinetic and equilibrium criteria, the bi-functionalized SiO_2 sorbent appears among the most efficient sorbents for Sr(II). It is noteworthy that, based on TGA analysis, the polymer content represents about 13.6% of the composite; this means that the functionalized polymer layer is highly efficient: sorption capacity represents about 10.15 mmol Sr g^{-1} functionalized polymer (not taking into account silica contribution to sorbent weight).

3.2.4. Sorption mechanism

The combination of data collected from the characterization sections and the sorption performances (pH effect and sorption isotherms) allows suggesting the main interactions involved in Sr(II) binding on $PAO_{20}MAA_{80}/SiO_2$ (Scheme 5). The main reactive groups on the sorbent consist of carboxylic acid and amidoxime moieties. At the optimum pH (close to neutrality), the pH_{PZC} value confirms the deprotonation of reactive groups. The slope analysis for pH effect (log plot of distribution coefficient *vs.* pH) does not allow identifying ion-exchange mechanism and strontium is supposed to be bound through chelation. FTIR analysis shows the contribution of carboxylic and amidoxime (through −NH, $-NH_2$, C═O and −OH functions). The molar ratio between carboxyl and amidoxime groups in $PAO_{20}MAA_{80}/SiO_2$ may explain the diversity of interaction modes, which is also confirmed by XPS analysis (identification of −N−Sr and −O−Sr bonds). Interactions may be of electrostatic and non-electrostatic nature due to deprotonation or electron delocalization of O- and N-based functional groups (Scheme 5).

3.2.5. Selectivity study

The selectivity of the sorbent for Sr(II) against other alkali and alkali-earth metal ions is shown in Fig. AM13. The fraction of strontium on the sorbent at equilibrium varies between 41% and 59% while varying the pH. The highest fractions are obtained at pH higher than 7. This is a first evidence that the sorbent has a marked preference for Sr (II). Indeed, the fraction in the solid is significantly enriched compared with the initial fraction in the solution (i.e., 20%). The cumulative

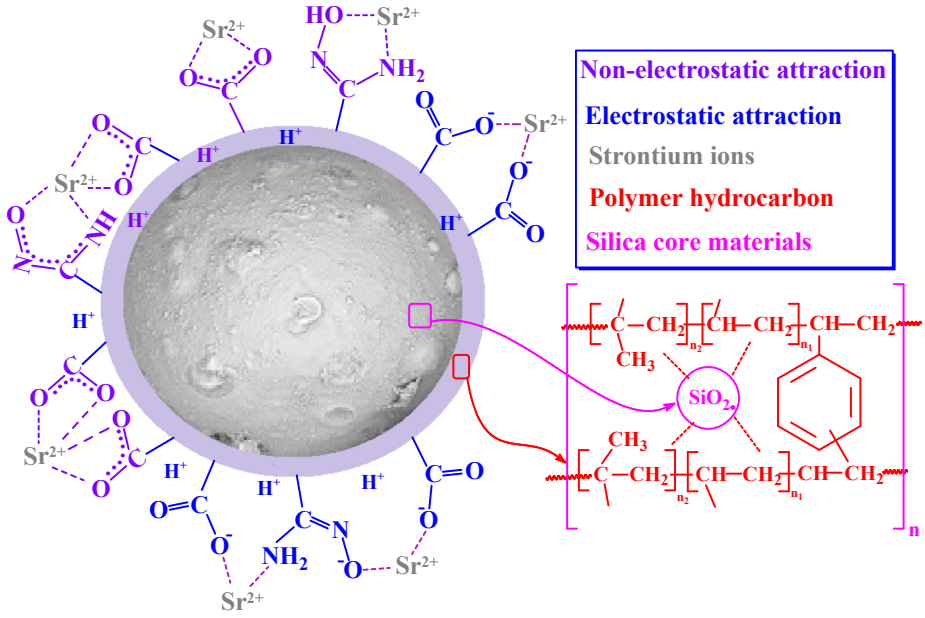

Scheme 5. Suggested mechanisms of Sr(II) sorption on bi-functionalized composite sorbent.

sorption capacity increases with up to pH 5.39 (1.39 mmol metal g^{-1}) and progressively decreases (down to 1.16 mmol metal g^{-1}) at pH 7.62.

On the other hand, consistently with the results obtained with single-component solutions, Sr(II) sorption continuously increases with pH and reaches (under selected experimental conditions) a sorption capacity close to 0.69 mmol Sr g^{-1} (in equilibrium with a residual concentration close to 0.513 mmol Sr g^{-1}). This is also consistent with the sorption capacity reached on the sorption isotherm (single-component) for the same residual concentration (i.e., ≈0.7 mmol Sr g^{-1} calculated from Freundlich and Sips equations, which provide the best fits of experimental isotherm in this concentration range). This means that the presence of co-ions in large excess does not impact the sorption capacity of Sr(II); although these co-ions can be bound to the sorbent (probably on other reactive groups). The cumulative sorption capacity reaches 1.16 mmol metal g^{-1} for a residual (cumulative) concentration close to 5.16 mmol metal L^{-1}. This concentration corresponds to the saturation plateau of the Sr(II) single-component isotherm at pH 8; the sorption capacity is found close to 1.36 mmol Sr g^{-1} (1.38 mmol Sr g^{-1} for simulated value, using the Langmuir equation). The multi-component solutions decreases by 16% the total sorption capacity compared with the corresponding residual concentration in mono-component solution. The sorbent is remarkably stable in sorption performance: Sr (II) sorption is hardly affected by the presence of competitor or co-ions and the total sorption capacity is of the same order of magnitude (though slightly lower than for Sr(II)-single solutions). It is noteworthy that at pH 5.39, Ca(II) sorption is relatively higher than the sorption of Ba(II), K(I) and Na(I).

Table AM10 shows the semi-quantitative analysis of $PAO_{20}MAA_{80}/SiO_2$ sorbent (surface) after being mixed with multi-component solutions at different pH values. These results confirm the relative selectivity of the sorbent for Sr(II). The atomic fraction at the surface of the sorbent for co-ions (i.e., Na(I), K(I), Ca(II) and Ba(II)) remains systematically below 0.08% while for Sr(II) the content increases with pH from 3 (i.e., 0.15%) up to 0.86–0.84% at pH 6–7, and increases again at pH 10 (up to 1.07%). The cumulative atomic fraction for co-ions ions does not exceed 0.22% at pH 6 to pH 8. In multi-component solutions, the sorbent shows a pH-response consistent with the results obtained with mono-component solutions.

Fig. 5 shows the selectivity coefficient ($SC_{Sr/metal} = D_{Sc}/D_{metal}$) of Sr (II) against Ba(II), Ca(II), K(I) and Na(I), at selected pH values. Regardless of the pH the SC is higher than 3; this confirms the preference of the sorbent for Sr(II) over selected metal cations. However, the SC is strongly affected by the pH. Indeed, above pH 5 the SC tends to increase, especially between 7 and 7.6. Against Ba(II), Ca(II), K(I) and Na (I), the SC reaches a maximum at pH 7.62 with values ranging between 10.7 against Na(I) up to 17.6 against K(I). $PAO_{20}MAA_{80}/SiO_2$ preference for Sr(II) against other alkali-earth metal ions (such as Ca(II) or Ba(II) is confirmed by the SC ranging between 12 and 14.2 at $pH_0 = 8$ ($pH_{eq} = 7.62$). At pH 6, where the differences are more marked between the different systems ($SC_{Sr/metal}$), the selectivity increases according: Ca(II) < Na(I) < Ba(II) < K(I). This ranking was compared with the relative values of different physicochemical properties of these elements (summarized in Table AM11). Actually, a relatively good correlation can be found between the $SC_{Sr/metal}$ parameters and the relative Pauling electronegativity ratios (χ_{metal}/χ_{Sr}), as shown in Fig. AM14.

Fig. AM15 provides complementary information on the comparison of sorption properties for selected metals. The $\log_{10}$ plots of the distribution ratios is plotted against equilibrium pH. The superimposition of the experimental points for Sr(II) sorption in multi-component

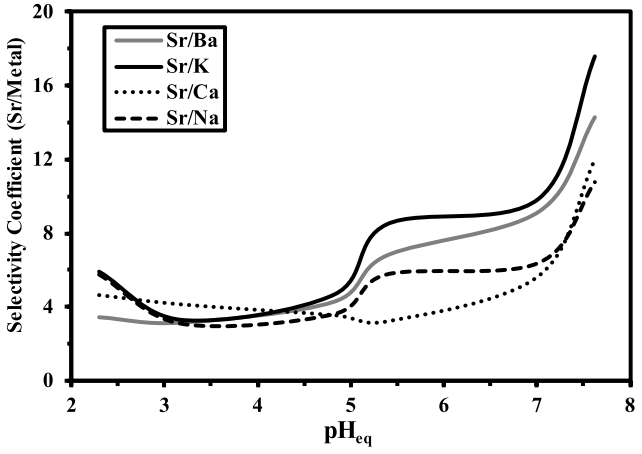

Fig. 5. Effect of pH on the selectivity coefficient for separation of Sr from mono- and divalent cations (multi-component equimolar concentrations; C_0 (individual): 1.3 mmol metal L^{-1}; SD: 0.125 g L^{-1}; agitation time: 48 h; agitation speed: 170 rpm; T: 22 ± 2 °C).

solutions with the curve obtained from mono-component solutions (filled symbols) confirms that the sorption of Sr(II) is hardly affected by the presence of these co-ions. In addition, the sorption levels (D_{Sc}) are significantly higher than those observed for the other co-ions. In the case of Sr(II), the curve is linear between pH 2 and 8 (and stabilizes above), while for the other metals a slope break is observed at the maximum between pH 5 and pH 6: this is consistent with the enhanced selectivity of the sorbent for Sr(II) at pH higher than 6. The ranking in sorption for alkali and alkali-earth metal ions at the optimum pH follows the series: Ca(II) > Na(I) > Ba(II) > K(I). This ranking cannot be directly correlated to the charge of metal ions. Table AM11 reports the main physicochemical characteristics of selected metal ions. Actually, the ranking does not follow the ionic radius of hydrated species (Shannon data) [57]: $Na(H_2O)_6^+$ (1.02 Å) < $Ca(H_2O)_8^+$ (1.12 Å) < $Ba(H_2O)_8^+$ (1.42 Å) < $K(H_2O)_8^+$ (1.51 Å). A better correlation is reported with Pauling electronegativity Ca(II)(1) > Na(I) (0.93) > Ba(II) (0.89) > K(I) (0.82). This confirms the influence of co-ion electronegativity on the selectivity of Sr(II) sorption using $PAO_{20}MAA_{80}/SiO_2$.

3.2.6. Metal desorption and sorbent recycling

Metal desorption is a critical step in the design of a sorption process since the recovery of the metal and the recycling or the sorbent are imperative for the competitiveness of the treatment. Fig. AM16 shows the perfect reproducibility of desorption kinetics. Fig. 6 shows the desorption kinetics for Sr(II) elution from loaded $PAO_{20}MAA_{80}/SiO_2$ using 0.5 M HCl solutions. The desorption profiles are very close for the different levels of Sr(II) loadings: the desorption is little slower with the low metal loading (i.e., 0.59 mmol Sr g^{-1}) while the profiles are superimposed for the higher loadings (i.e., 1.21 and 1.36 mmol Sr g^{-1}). The sorption kinetic profiles were not superimposed (Fig. 2). Complete metal desorption occurs within 20–30 min of contact; this is shorter than the equilibrium time required for metal sorption (40–60 min). The PFORE better fits desorption kinetics than the PSORE (especially considering the complete desorption for PFORE while PSORE modeling does not achieve complete metal elution); this is another significant difference with the sorption step, where the differences between the models were less significant. The apparent rate coefficient (for PFORE) are little higher than the values obtained during sorption step (Tables 2 and 5).

Table 6 compares the performances of sorption and desorption for Sr(II) removal using $PAO_{20}MAA_{80}/SiO_2$ for five successive cycles. The desorption of Sr(II) from metal-loaded resin is very efficient and stable for 5 cycles using 0.5 M HCl solution as the eluent: metal desorption is completely achieved for, at least, the first five cycles. The sorption efficiency progressively decreases (from 58.3 ± 0.5% to 54.5 ± 0.1%). This 6.5%-loss in sorption efficiency (despite the complete desorption of the metal), is probably due to a partial degradation of the sorbent. This is an important parameter for higher number of recycling cycles. However, the combined sorption/desorption performances are globally very attractive for the selective recovery of Sr(II) from complex solutions.

3.2.7. Dynamic sorption – fixed-bed column

The resins were applied in fixed-bed column for dynamic sorption (Fig. 7 and Fig. AM17). The breakthrough curves are correctly fitted by the Thomas equation [55] (Table 7). The reproducibility of breakthrough curves is clearly demonstrated by the superposition of experimental profiles. The comparison of linear (LR) and non-linear (NLR) regression analysis shows that the non-linear regression analysis gives a better mathematical fit. Increasing the flow rate (and superficial velocity) improves the quality of the fit. The calculated sorption capacity is consistent with the experimental values (little overestimation, by less than 4% for LR); in the case of NLR, the sorption capacity is more overestimated (despite the better global fit of experimental profiles). Surprisingly, the sorption capacity linearly decreases with superficial velocity (while using the same amount of sorbent and the same initial metal concentration); this means that the saturation of the sorbent is not achieved. The expected sorption capacity at equilibrium is deduced from the sorption isotherms (close to 0.74 mmol Sr g^{-1}). The sorption capacities obtained in dynamic system are systematically much lower than the expected value, from 0.247–0.270 to 0.535–0.544 mmol Sr g^{-1}, depending on the flow rate. This is another confirmation that the sorbent is not fully saturated. Ang et al. [96] observed close values for the saturation capacities in the case of the sorption of anesthetic gaseous agent on activated carbon when varying the flow rate. The rate coefficient k_T (L $mmol^{-1}h^{-1}$) linearly increases with the superficial velocity (between 0.32 and 2.390 L $mmol^{-1}h^{-1}$ for LR; between 0.246 and 2.09 $mmol^{-1}h^{-1}$ for NLR); consistently with the conclusions raised by Ang et al. [96]. In the case of base metals using melamine-functionalized SBA-15 mesoporous silica, Shabazi et al. [97] reported that a maximum sorption capacity was obtained at intermediary flow rate; the relevant sorption capacities were also lower than the corresponding sorption capacities obtained in batch mode. Araneda et al. [98] investigated the dynamic sorption of copper on extractant-immobilized microcapsules; they also observed a significant decrease of the sorption capacity calculated by the Thomas model with increasing the flow rate. The rate coefficient also increased with the flow rate.

3.2.8. Sr(II) sorption from seawater

The semi-quantitative EDX analysis of seawater treatment by sorption onto $PAO_{20}MAA_{80}/SiO_2$ is reported in Table AM12 for different pH values. The SiO_2 core is appearing through the two major peaks of EDX spectra for Si and O elements that represent between 69 and 77% of the sorbent (atomic fractions, AF). The polymer coating is associated to C content, which increases from 9 to 12% (AF) when the pH increases from 4 to 8–10: this C increases may be explained by the formation of carbonate complexes or the accumulation of organic materials

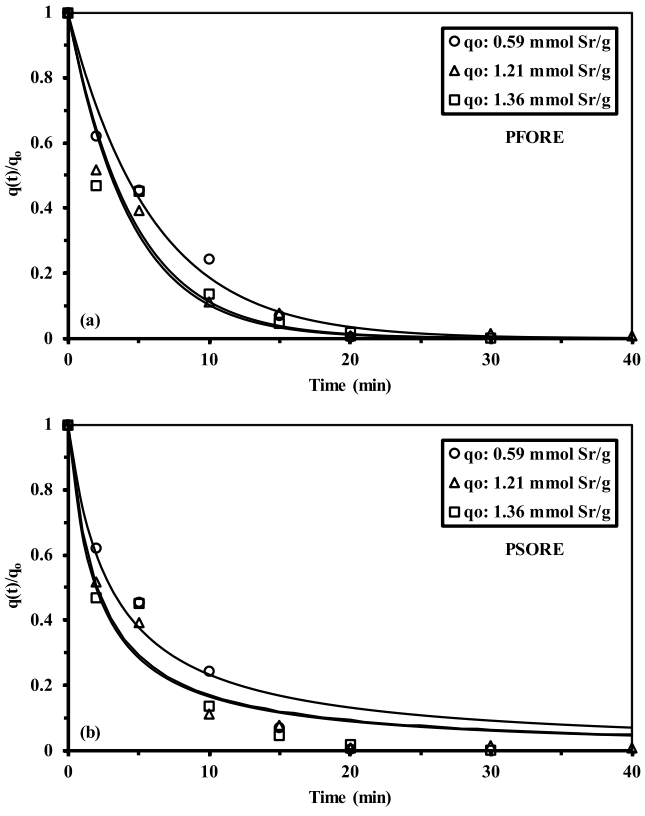

Fig. 6. Sr(II) desorption kinetics from metal-loaded $PAO_{20}MAA_{80}/SiO_2$ – Modeling with the PFORE (a) and the PSORE (b) (sorbent collected from uptake kinetic experiments; desorption conditions: 0.5 M HCl as eluent; SD: 1 g L^{-1}; agitation speed: 170 rpm; T: 22 ± 2 °C).

Table 5
Parameters of kinetic models for Sr(II) desorp tion from metal-loaded $PAO_{20}MAA_{80}/SiO_2$ using the PFORE and PSORE fits [54].

Loaded conc. (mmol Sr g^{-1})	Model	PFORE		PSORE		
	Parameter	k_{D1} (min^{-1})	R^2	β_2	k_{D2} (min^{-1})	R^2
Run #1 – 0.590		0.171	0.985	0.989	0.319	0.970
Run #2 – 0.591		0.163	0.970	0.990	0.327	0.964
1.21		0.228	0.979	0.992	0.492	0.973
1.36		0.218	0.949	1.000	0.484	0.951

PFORE: $\frac{q(t)}{q_0} = e^{-k_{D1}t}$ with: k_{D1} the apparent rate coefficient for desorption (min^{-1}) PSORE: $\frac{q(t)}{q_0} = \frac{1}{\beta_2 + k_{D2}t}$ with: k_{D2} the apparent rate coefficient for desorption (min^{-1}) and β_2 (dimensionless) the constant for PSORE (in desorption).

Table 6
Sr(II) sorption and desorption efficiencies for $PAO_{20}MAA_{80}/SiO_2$ sorbent recycling.

Cycle #	Sorption efficiency (%)		Desorption efficiency (%)	
	Average	S.D.	Average	S.D.
1	58.3	0.5	100.1	0.4
2	57.0	0.4	100.3	0.6
3	56.4	0.2	100.3	0.5
4	54.8	0.2	100.0	0.6
5	54.5	0.0	100.2	0.3

Experimental conditions – Sorption: C_0: 51 mg Sr L^{-1} = 0.582 mmol Sr L^{-1}; pH: 8.05; SD: 0.61 g L^{-1}; time: 24 h; T: 22 ± 2 °C; agitation speed: 170 rpm/ Desorption: eluent: 1 M HCl; SD: 1.5 g L^{-1}; time: 2 h T: 22 ± 2 °C; agitation speed: 170 rpm.

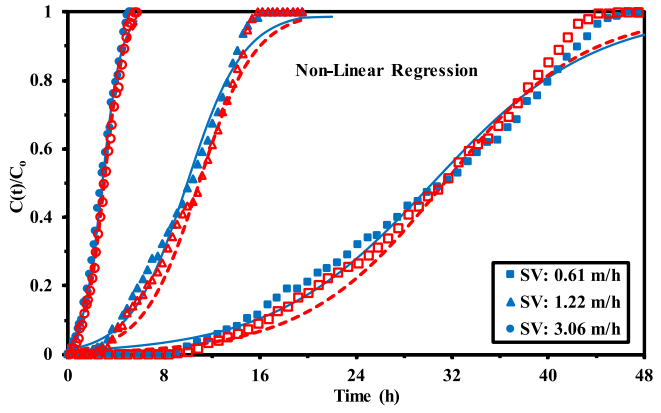

Fig. 7. Breakthrough curves for the sorption of Sr(II) using $PAO_{20}MAA_{80}/SiO_2$ – effect of superficial velocity (sorbent weight 400 mg; pH_0:8); modeling of experimental breakthrough curves with the Thomas equation; Run #1 (closed symbols and solid lines) C_0: 53 mg Sr L^{-1} = 0.605 mmol Sr L^{-1}; Run #2 (open symbols and dashed lines) C_0: 54 mg Sr L^{-1} = 0.615 mmol Sr L^{-1}; parameters determined by non-linear regression analysis).

contained in seawater that can bound to the sorbent active sites. Similarly, for S element: the content increases in neutral or alkaline solutions, probably associated to the binding of sulfate, hydrogen sulfate or metal sulfate. The amount of N element (in the range 4.64–6.34 %, AF) is due to amidoxime moiety. Strontium content increases from 0.04% at pH 4 to 0.54–0.46% at pH 8–10. This is consistent with the previous results obtained with synthetic solutions. Consistently with the trends observed for multi-component synthetic solutions, Ca(II) sorption hardly varies between 0.22 and 0.37%, K(I) between 0.01 and 0.15%, Mg(II) between 0.16 and 0.36 % (increasing with pH). The case of Na(I) is little different: Na content continuously decreases with pH (from 3.22 to 0.04%). Other elements are identified on EDX spectra:

Table 7
Modeling of breakthrough curves for the sorption of Sr(II) using $PAO_{20}MAA_{80}/SiO_2$ at different flow rates (Q, mL min^{-1}; Superficial flow velocity, SV, m h^{-1}) – Parameters of the Thomas model [55].

Q	SV	Run	$q_{exp.}$ (mmol Sr g^{-1})	Regr.	q_{model} (mmol Sr g^{-1})	k_T (L $mmol^{-1}h^{-1}$)	R^2
0.2	0.61	#1	0.535	L	0.533	0.320	0.975
				NL	0.551	0.246	0.989
		#2	0.544	L	0.527	0.357	0.978
				NL	0.562	0.279	0.994
0.4	1.22	#1	0.346	L	0.357	0.829	0.984
				NL	0.359	0.702	0.993
		#2	0.372	L	0.381	0.843	0.983
				NL	0.403	0.705	0.992
1.0	3.06	#1	0.247	L	0.258	2.328	0.993
				NL	0.256	2.090	0.996
		#2	0.270	L	0.278	2.390	0.994
				NL	0.279	2.057	0.997

$q_{th.}$ = 0.707 mmol Sr g^{-1}; L: linear regression, NL: non-linear regression analysis.

Thomas equation: $\ln\left(\frac{C_0}{C(t)} - 1\right) = \frac{k_T q_{eq} m}{Q} - k_T C_0 t$.

Where k_T is the Thomas rate constant (L $mg^{-1}h^{-1}$), q_{eq} the sorption capacity at equilibrium (mmol Sr g^{-1}), m the amount of sorbent (g), Q the flow rate (L h^{-1}); t the time (h), C_0 and C(t): the inlet and outlet concentrations, respectively.

such as B(III), Mo(VI) and Ru(III). A special attention has been paid to the sorption kinetics of this series of metals or elements at different pH values. Fig. AM18 compares the kinetic profiles for traces removal: for B (III) and Sr(II) the residual concentration progressively decreases up to 48 h; the sorption of Mo(VI) is much faster (a pseudo-equilibrium, corresponding to 90% of total sorption, is reached within 6–10 h). For the other (major) elements (not shown), at much higher concentration, the variation of the concentration in the solution is relatively weak (less than 3%, and even less than 1% for Na(I) and K(I)); the equilibrium is reached within 12–24 h.

The sorption capacities are directly controlled by their metal concentration in seawater (Tables AM13 and AM14) and the pH of the solution: sorption capacities increase with pH (consistently with experiments on synthetic solutions), essentially between pH 4 and pH 8. The cumulative sorption capacity increases up to 8.84 mmol metal g^{-1} at pH 10. The Sr(II) sorption capacity increases from 0.071 to 0.103 mmol Sr g^{-1} when the pH increases from 8 to 10. Compared to the sorption isotherm obtained with synthetic pure solution, for a residual concentration close to 0.0104 mmol Sr L^{-1} at pH 8, according the Sips equation (which fits the most closely the isotherm at low metal concentration), the expected sorption capacity should be close to 0.093 mmol Sr g^{-1}. This means that the loss in sorption capacity in such a complex solution does not exceed 25%.

The most significant enrichments (compared with initial metal concentrations: q_{eq}/C_0, L g^{-1}) are observed for trace elements such as Sr(II) (up to 3.32 L g^{-1}), Mo(VI) (up to 3.16 L g^{-1}) and B(III) (up to 1.37 L g^{-1}) at pH_0 10, while for the other metals the enrichment factor does not exceed 0.175 L g^{-1}. The values of distribution ratio (D, L g^{-1}) are also summarized in Table AM14: highest D values are observed at pH 10 for Sr(II) > Mo(VI) and B(III). The selectivity coefficients for Sr over co-ions are reported in Fig. AM19. The SC increases with time and pH. The systems are difficultly comparable due to the large excess in the concentration of the major elements; however, these data offer an easy comparison tool for highlighting the preference of the sorbent for Sr(II) over the co-ions. Highest SCs are observed according the sequence: Na (I) (8 4 6) > K(I) (2 3 8) > Mg(II) (1 9 2) > Ca(II) (1 0 3) > Ru(III) (62) > B(III) (5). On the opposite hand, the sorbent has a little preference for Mo(VI) against Sr(II) ($SC_{Sr/Mo} < 1$) at pH 4 and 8; at pH 10, the sorbent does not show selectivity between the two metal ions.

These results show that in such a complex solution as seawater, the

sorbent maintains:

(a) good sorption properties for Sr(II),
(b) high affinity for other trace metal ions (B(III) and more specifically Mo(VI)), and
(c) strong enrichment factor and high relative distribution ratios for these trace metal ions (despite huge excess of Na(I), Mg(II), L(I) and Ca(II)).

4. Conclusion

The combined grafting of both polyacrylic and amidoxime groups on silica microspheres (size: around 120 μm) allows enhancing the sorption properties of the composite for Sr(II), compared with monofunctional sorbents (bearing solely PMAA or PAO moieties). However, the comparison of sorption performances shows that maximum sorption efficiency for Sr(II) is reached for specific substitution grade (i.e., corresponding to $PAO_{20}MAA_{80}/SiO_2$ composite sorbent). The sorbents are characterized by elemental analysis (3.36–7.8 mmol N g^{-1}), semi-quantitative EDX analysis, textural properties (SSA: 62–69 m^2 g^{-1}), TGA (about 13.6% weight loss at 875 °C, representing the hydrocarbon coating fraction), pH_{PZC} (6.42–6.51 for $PAO_{20}MAA_{80}/SiO_2$ composite sorbent). FTIR and XPS analyses confirm the appearance of functional groups on the polymer coating layer of composite materials, consistently with suggested synthesis procedures. In addition, the changes in spectra confirm the contribution of amine, hydroxyl/carboxyl groups in the binding of Sr(II) on the composite sorbent.

Optimum sorption occurs at pH 8. The uptake is relatively fast: equilibrium is reached within 40–60 min of contact. The sorption is fitted by the pseudo-first order rate equation: apparent rate coefficient varies in the range 0.09–10.17 min^{-1}. The maximum sorption capacity is closed to 1.38 mmol Sr g^{-1} (10.15 mmol Sr g^{-1} when reported in function of the effective amount of functionalized polymer in the composite); the isotherms are equally fitted by the Langmuir (capacity at saturation of the monolayer close to 1.57 mmol Sr g^{-1}) and the Sips equations. These sorption capacities are among the most promising compared with available literature data. The recycling of the sorbent is verified over 5 cycles of sorption and desorption: 1 M HCl solution offers complete, fast (equilibrium within 20 min) and stable desorption of Sr(II) while the sorption efficiency slightly decreases (less than 7% at the fifth cycle). In equimolar multi-component solutions, the sorption is selective for Sr(II) over alkali and alkali earth metal ions. This is confirmed by the tests performed on Sr(II) sorption in seawater: high distribution ratio (in the range 1–10 L g^{-1}) are observed for Sr(II) and B(III) or Mo(VI), despite the huge excess of alkali and alkali-earth metal ions. In dynamic systems (i.e., fixed-bed column), the breakthrough curves for Sr(II) sorption are finely fitted by the Thomas model; although the sorption capacity is significantly under evaluated compared with static systems.

Declaration of Competing Interest

The authors declare that they have no known competing financial interests or personal relationships that could have appeared to influence the work reported in this paper.

Acknowledgements

M. R. acknowledges the China Scholarship Council (CSC, Grant N 2018DFH009893) for MSc fellowship. Y. W. thanks the support of NSFC Projects (No. 11675102, No. 11975082, U1967218), Science and Technology Major project of Guangxi Province (AA17204100, AA18118030). E.G. and M.F.H acknowledge Institut Francais d'Egypte for supporting the collaboration between IMT-Mines Ales and Nuclear Materials Authority, and IMHOTEP project "MetalValor" (funded by Ministère des Affaires Etrangères and Ministère de l'Enseignement Supérieur et de la Recherche; and by Science and Technology Development Fund from Egyptian Academy of Science and Technology).

Appendix A. Supplementary data

Supplementary data to this article can be found online at https://doi.org/10.1016/j.cej.2020.125220.

References

[1] K. Hirose, P.P. Povinec, Cs-137 and Sr-90 in surface waters of the Sea of Japan: Variations and the Fukushima Dai-ichi Nuclear Power Plant accident impact, Mar. Pollut. Bull. 146 (2019) 645–652.
[2] R. Querfeld, A.-E. Pasi, K. Shozugawa, C. Vockenhuber, H.-A. Synal, P. Steier, G. Steinhauser, Radionuclides in surface waters around the damaged Fukushima Daiichi NPP one month after the accident: evidence of significant tritium release into the environment, Sci. Total Environ. 689 (2019) 451–456.
[3] M. Konno, Y. Takagai, Determination and comparison of the strontium-90 concentrations in topsoil of fukushima prefecture before and after the Fukushima Daiichi nuclear accident, ACS Omega 3 (2018) 18028–18038.
[4] S.H. Kim, H. Lee, S.H. Lee, I. Kim, Distribution and accumulation of artificial radionuclides in marine products around Korean Peninsula, Mar. Pollut. Bull. 146 (2019) 521–531.
[5] T. Shubair, O. Eljamal, A. Tahara, Y. Sugihara, N. Matsunaga, Preparation of new magnetic zeolite nanocomposites for removal of strontium from polluted waters, J. Mol. Liq. 288 (2019).
[6] L.Y. Wu, G.H. Zhang, Q.Z. Wang, L. Hou, P. Gu, Removal of strontium from liquid waste using a hydraulic pellet co-precipitation microfiltration (HPC-MF) process, Desalination 349 (2014) 31–38.
[7] J.G. Cao, P. Gu, J. Zhao, D. Zhang, Y. Deng, Removal of strontium from an aqueous solution using co-precipitation followed by microfiltration (CPMF), J. Radioanal. Nucl. Chem. 285 (2010) 539–546.
[8] J.N. Sharma, P.N. Khan, P.S. Dhami, P. Jagasia, V. Tessy, C.P. Kaushik, Separation of strontium-90 from a highly saline high level liquid waste solution using 4,4′(5′)-di-tert-butyldicyclohexano-18-crown-6 + isodecyl alcohol/n-dodecane solvent, Sep. Purif. Technol. 229 (2019).
[9] Y. Xu, Y. Gao, Y. Zhou, C. Fan, H. Hou, M. Zhang, Extraction behavior of strontium from nitric acid medium with N, N′-dimethyl-N, N′-dioctyldiglycolamide, Solvent Extr. Ion Exch. 35 (2017) 507–518.
[10] R. Yavari, Y.D. Huang, A. Mostofizadeh, Sorption of strontium ions from aqueous solutions by oxidized multiwall carbon nanotubes, J. Radioanal. Nucl. Chem. 285 (2010) 703–710.
[11] C.K. Aslani, F. Belloni, B. Cetinkaya, V.V. Rondinella, Sorption studies of strontium on carbon nanotubes using the Box-Behnken design, Radiochim. Acta 102 (2014) 931–940.
[12] S. Hayakawa, S. Matsubara, Y. Sumi, S. Yamamoto, N. Kawamura, T. Nonami, Caesium and strontium adsorption ability of activated bamboo charcoal, Int. J. Nanotechnol. 15 (2018) 683–688.
[13] S. Kobayashi, K. Noda, H. Shibata, S. Matsubara, N. Kawamura, T. Nonami, Rice hull charcoal for adsorption of cesium and strontium in aqueous solution, Mater. Trans. 60 (2019) 458–463.
[14] L. Qiu, J.D. Feng, Y.D. Dai, S.Q. Chang, Biosorption of strontium ions from simulated high-level liquid waste by living *Saccharomyces cerevisiae*, Environ. Sci. Pollut. Res. 25 (2018) 17194–17206.
[15] D. Song, S.-J. Park, H.W. Kang, S.B. Park, J.-I. Han, Recovery of lithium(I), strontium(II), and lanthanum(III) using Ca-alginate beads, J. Chem. Eng. Data 58 (2013) 2455–2464.
[16] J. Maresova, M. Pipiska, M. Rozloznik, M. Hornik, L. Remenarova, J. Augustin, Cobalt and strontium sorption by moss biosorbent: Modeling of single and binary metal systems, Desalination 266 (2011) 134–141.
[17] K.V. Mahindrakar, V.K. Rathod, Utilization of banana peels for removal of strontium (II) from water, Environ. Technol. Innovation 11 (2018) 371–383.
[18] Y.M. Hu, X. Guo, C. Chen, J.L. Wang, Algal sorbent derived from *Sargassum horneri* for adsorption of cesium and strontium ions: equilibrium, kinetics, and mass transfer, Appl. Microbiol. Biotechnol. 103 (2019) 2833–2843.
[19] M. Galambos, J. Kufcakova, P. Rajec, Sorption of strontium on Slovak bentonites, J. Radioanal. Nucl. Chem. 281 (2009) 347–357.
[20] W. Janusz, E. Skwarek, Study of sorption processes of strontium on the synthetic hydroxyapatite, Adsorption – J. Int. Ads. Soc. 22 (2016) 697–706.
[21] D. Alby, C. Charnay, M. Heran, B. Prelot, J. Zajac, Recent developments in nanostructured inorganic materials for sorption of cesium and strontium: Synthesis and shaping, sorption capacity, mechanisms, and selectivity – a review, J. Hazard. Mater. 344 (2018) 511–530.
[22] X. Xia, J. Shen, F. Cao, C.J. Wang, M. Tang, Q.Y. Zhang, S.S. Wei, A facile synthesis of hydroxyapatite for effective removal strontium ion, J. Hazard. Mater. 368 (2019) 326–335.
[23] R. Zuo, L. Meng, X. Guan, J.S. Wang, J. Yang, Y.H. Lin, Removal of strontium from aqueous solutions by acrylamide-modified attapulgite, J. Radioanal. Nucl. Chem. 319 (2019) 1207–1217.
[24] R. Zuo, S. Jin, J. Yang, J. Wang, X. Guan, L. Meng, Y. Teng, M. Chen, Removal of

strontium from aqueous solutions by sodium dodecyl sulfate-modified palygorskite, J. Radioanal. Nucl. Chem. 321 (2019) 151–159.
[25] H.S. Hassan, A.M. El-Kamash, H.A.-S. Ibrahim, Evaluation of hydroxyapatite/poly (acrylamide-acrylic acid) for sorptive removal of strontium ions from aqueous solution, Environ. Sci. Pollut. Res. 26 (2019) 25641–25655.
[26] H.J. Hong, B.G. Kim, J. Ryu, I.S. Park, K.S. Chung, S.M. Lee, J.B. Lee, H.S. Jeong, H. Kim, T. Ryu, Preparation of highly stable zeolite-alginate foam composite for strontium(Sr-90) removal from seawater and evaluation of Sr adsorption performance, J. Environ. Manage. 205 (2018) 192–200.
[27] S.Y. Wang, S.Y. Ning, W. Zhang, S.C. Zhang, J. Zhou, X.P. Wang, Y.Z. Wei, Synthesis of carboxyl group functionalized silica composite resin for strontium removal, Mater. Des. 185 (2020) 9.
[28] R.O.A. Rahman, O.A.A. Moamen, N. Abdelmonem, I.M. Ismail, Optimizing the removal of strontium and cesium ions from binary solutions on magnetic nanozeolite using response surface methodology (RSM) and artificial neural network (ANN), Environ. Res. 173 (2019) 397–410.
[29] T. Kawamura, T. Ito, S.Y. Kim, Adsorption and separation behavior of strontium and yttrium using a silica-based CMPO adsorbent, J. Radioanal. Nucl. Chem. 320 (2019) 9–14.
[30] T.T. Li, F. He, Y.D. Dai, Prussian blue analog caged in chitosan surface-decorated carbon nanotubes for removal cesium and strontium, J. Radioanal. Nucl. Chem. 310 (2016) 1139–1145.
[31] A.V. Voronina, V.S. Semenishchev, Mechanism of strontium sorption by the mixed nickel-potassium ferrocyanide based on hydrated titanium dioxide, J. Radioanal. Nucl. Chem. 307 (2016) 577–590.
[32] O. Eljamal, T. Shubair, A. Tahara, Y. Sugihara, N. Matsunaga, Iron based nanoparticles-zeolite composites for the removal of cesium from aqueous solutions, J. Mol. Liq. 277 (2019) 613–623.
[33] T. Shubair, O. Eljamal, A.M.E. Khalil, A. Tahara, N. Matsunaga, Novel application of nanoscale zero valent iron and bimetallic nano-Fe/Cu particles for the treatment of cesium contaminated water, J. Environ. Chem. Eng. 6 (2018) 4253–4264.
[34] K. Mulani, V. Patil, N. Chavan, K. Donde, Adsorptive removal of strontium(II) using macroporous poly(AGE-*co*-EGDMA) beads modified with resorcin 4 arene, Bull. Mater. Sci. 42 (2019).
[35] N.N. Basargin, E.V. Demina, V.Y. Anikin, I.B. Kometiani, Strontium(II) sorption by complexing o-hydroxy-azo-o'-hydroxy functionalized polystyrene polymer sorbents, Russ. J. Inorg. Chem. 56 (2011) 2019–2023.
[36] V.Y. Anikin, N.N. Basargin, O.V. Tarasova, Y.G. Rozovskii, Strontium(II) sorption by complexing polymeric sorbents with various structures, Russ. J. Inorg. Chem. 54 (2009) 1507–1511.
[37] P. Asgari, S.H. Mousavi, H. Aghayan, H. Ghasemi, T. Yousefi, Nd-BTC metal-organic framework (MOF); synthesis, characterization and investigation on its adsorption behavior toward cesium and strontium ions, Microchem. J. 150 (2019) 104188, https://doi.org/10.1016/j.microc.2019.104188.
[38] H.J. Hong, J. Ryu, I.S. Park, T. Ryu, K.S. Chung, B.G. Kim, Investigation of the strontium (Sr(II)) adsorption of an alginate microsphere as a low-cost adsorbent for removal and recovery from seawater, J. Environ. Manage. 165 (2016) 263–270.
[39] M. Piechowicz, C.W. Abney, X. Zhou, N.C. Thacker, Z. Li, W. Lin, Design, synthesis, and characterization of a bifunctional chelator with ultrahigh capacity for uranium uptake from seawater simulant, Ind. Eng. Chem. Res. 55 (2016) 4170–4178.
[40] A.F. Shaaban, T.Y. Mohamed, D.A. Fadel, N.M. Bayomi, Removal of Ba(II) and Sr (II) ions using modified chitosan beads with pendent amidoxime moieties by batch and fixed bed column methods, Desalin. Water Treat. 82 (2017) 131–145.
[41] Y. Wei, K.A.M. Salih, S. Lu, M.F. Hamza, T. Fujita, T. Vincent, E. Guibal, Amidoxime functionalization of algal/polyethyleneimine beads for the sorption of Sr(II) from aqueous solutions, Molecules 24 (2019) 3893.
[42] A.M.A. Nada, N.A. El-Wakil, M.L. Hassan, A.M. Adel, Differential adsorption of heavy metal ions by cotton stalk cation-exchangers containing multiple functional groups, J. Appl. Polym. Sci. 101 (2006) 4124–4132.
[43] S.A. Younis, M.M. Ghobashy, G. Bassioni, A.K. Gupta, Tailored functionalized polymer nanoparticles using gamma radiation for selected adsorption of barium and strontium in oilfield wastewater, Arabian J. Chem. (2018).
[44] Y. Dai, R. Lv, D. Huang, Q. Tao, Sorption of uranium on a bifunctional polymer of diethylenetriaminepentaacetic acid cross-linked beta-cyclodextrin in the presence of humic acid: Kinetics, isotherms, and thermodynamics, Water Air Soil Pollut. 229 (2018).
[45] K.V. Syamala, K.A. Venkatesan, M.P. Antony, P.R.V. Rao, Kinetics of Eu(III) extraction in macroporous bifunctional phosphinic acid resin, Sep. Sci. Technol. 51 (2016) 2001–2007.
[46] S.D. Alexandratos, X.P. Zhu, M. Florent, R. Sellin, Polymer-supported bifunctional amidoximes for the sorption of uranium from seawater, Ind. Eng. Chem. Res. 55 (2016) 4208–4216.
[47] Y. Wei, J. Qian, L. Huang, D. Hua, Bifunctional polymeric microspheres for efficient uranium sorption from aqueous solution: synergistic interaction of positive charge and amidoxime group, RSC Adv. 5 (2015) 64286–64292.
[48] R.J. Qu, Y. Zhang, W.W. Qu, C.M. Sun, J. Chen, Y. Ping, H. Chen, Y.Z. Niu, Mercury adsorption by sulfur- and amidoxime-containing bifunctional silica gel based hybrid materials, Chem. Eng. J. 219 (2013) 51–61.
[49] X. Wang, L. Yuan, Y. Wang, Z. Li, J. Lan, Y. Liu, Y. Feng, Y. Zhao, Z. Chai, W. Shi, Mesoporous silica SBA-15 functionalized with phosphonate and amino groups for uranium uptake, Science China Chem. 55 (2012) 1705–1711.
[50] L. Tofan, C. Paduraru, I. Cretescu, A. Ceica, V. Neagu, Chelating sorbent containing two types of functional groups – hydroxamic acid and amidoxime for lead (II) ions effluent management, Environ. Eng. Manage. J. 9 (2010) 113–118.
[51] S.E. Kudaibergenov, Physicochemical, complexation and catalytic properties of polyampholyte cryogels, Gels (Basel, Switzerland) 5 (2019).
[52] M.V. Lopez-Ramon, F. Stoeckli, C. Moreno-Castilla, F. Carrasco-Marin, On the characterization of acidic and basic surface sites on carbons by various techniques, Carbon 37 (1999) 1215–1221.
[53] O. Falyouna, O. Eljamal, I. Maamoun, A. Tahara, Y. Sugihara, Magnetic zeolite synthesis for efficient removal of cesium in a lab-scale continuous treatment system, J. Colloid Interface Sci. 571 (2020) 66–79.
[54] N.K. Lazaridis, T.A. Pandi, K.A. Matis, Chromium(VI) removal from aqueous solutions by Mg-Al-CO_3 hydrotalcite: Sorption-desorption kinetic and equilibrium studies, Ind. Eng. Chem. Res. 43 (2004) 2209–2215.
[55] D. Tiwari, S.M. Lee, Novel hybrid materials in the remediation of ground waters contaminated with As(III) and As(V), Chem. Eng. J. 204 (2012) 23–31.
[56] Y. Li, F.X. Song, L. Cheng, J. Qian, Q.L. Chen, Functionalized large-pore mesoporous silica microparticles for gefitinib and doxorubicin codelivery, Materials 12 (2019).
[57] I. Persson, Hydrated metal ions in aqueous solution: how regular are their structures? Pure Appl. Chem. 82 (2010) 1901–1917.
[58] T. Yu, J. Lin, J. Xu, T. Chen, S. Lin, X. Tian, Novel polyacrylonitrile/Na-MMT/silica nanocomposite: co-incorporation of two different form nano materials into polymer matrix, Compos. Sci. Technol. 67 (2007) 3219–3225.
[59] L.W. Ji, C. Saquing, S.A. Khan, X.W. Zhang, Preparation and characterization of silica nanoparticulate-polyacrylonitrile composite and porous nanofibers, Nanotechnology 19 (2008) 9.
[60] I.A. Khan, T. Yasin, H. Hussain, Development of amidoxime functionalized silica by radiation-induced grafting, J. Appl. Polym. Sci. 134 (2017).
[61] D.N. Clausen, I.M.R. Pires, C.R.T. Tarley, Improved selective cholesterol adsorption by molecularly imprinted poly(methacrylic acid)/silica (PMAA-SiO2) hybrid material synthesized with different molar ratios, Mater. Sci. Eng., C 44 (2014) 99–108.
[62] M.S. Iqbal, Y. Jamil, T. Kausar, M. Akhtar, Thermal degradation study of glycidyl methacrylate acrylonitrile copolymers, J. Therm. Anal. Calorim. 96 (2009) 225–233.
[63] J. Zhang, Z. Lu, M. Wu, Q. Wu, J. Yang, Facile fabrication of poly(acrylic acid) hollow nanogels via in situ Pickering miniemulsion polymerization, Polym. Chem. 6 (2015) 6125–6128.
[64] Z. Zhao, X. Xie, Z. Wang, Y. Tao, X. Niu, X. Huang, L. Liu, Z. Li, Immobilization of *Lactobacillus rhamnosus* in mesoporous silica-based material: an efficiency continuous cell-recycle fermentation system for lactic acid production, J. Biosci. Bioeng. 121 (2016) 645–651.
[65] I. Ramalla, R.K. Gupta, K. Bansal, Effect on superhydrophobic surfaces on electrical porcelain insulator, improved technique at polluted areas for longer life and reliability, Int. J. Eng. Technol. 4 (2015) 509–519.
[66] S. Lu, L. Chen, M.F. Hamza, C. He, X. Wang, Y. Wei, E. Guibal, Amidoxime functionalization of a poly(acrylonitrile)/silica composite for the sorption of Ga (III) – application to the treatment of Bayer liquor, Chem. Eng. J. 368 (2019) 459–473.
[67] N. Liu, R.A. Assink, B. Smarsly, C.J. Brinker, Synthesis and characterization of highly ordered functional mesoporous silica thin films with positively chargeable-NH_2 groups, Chem. Commun. 9 (2003) 1146–1147.
[68] X. Zhang, R.F. Guan, D.Q. Wu, K.Y. Chan, Enzyme immobilization on amino-functionalized mesostructured cellular foam surfaces, characterization and catalytic properties, J. Mol. Catal. B: Enz. 33 (2005) 43–50.
[69] A.M. Atta, A.A.H. Abdel-Rahman, M.F. Hamza, I.E. El Aassy, F.Y. Ahmed, Effect of crosslinker chemical structure and monomer compositions on adsorption of uranium (VI) ions based on reactive crosslinked acrylamidoxime acrylic acid resins, J. Dispersion Sci. Technol. 33 (2012) 490–496.
[70] J. Coates, Interpretation of infrared spectra, a practical approach, Encyclopedia of Analytical Chemistry, John Wiley & Sons, Ltd., 2006, pp. 1–23.
[71] M.F. Hamza, Y. Wei, E. Guibal, Quaternization of algal/PEI beads (a new sorbent): characterization and application to scandium recovery from aqueous solutions, Chem. Eng. J. 383 (2020) 123210.
[72] Y. Wei, S. Wei, C. Liu, T. Chen, Y. Tang, J. Ma, K. Yin, S. Luo, Efficient removal of arsenic from groundwater using iron oxide nanoneedle array-decorated biochar fibers with high Fe utilization and fast adsorption kinetics, Water Res. 167 (2019).
[73] N.B. Colthup, L.H. Daly, S.E. Wiberley, Introduction to Infrared and Raman Spectroscopy, third. ed., Academic Press Inc, San Diego, CA (USA), 1990, p. 560.
[74] M.F. Hamza, A. Gamal, G. Hussein, M.S. Nagar, A.A.H. Abdel-Rahman, Y. Wei, E. Guibal, Uranium(VI) and zirconium(IV) sorption on magnetic chitosan derivatives – effect of different functional groups on separation properties, J. Chem. Technol. Biotechnol. 94 (2019) 3866–3882.
[75] A.A.H. Abdel-Rahman, I.E.E. El-Aassy, Y.A. Fadia, M.F. Hamza, Studies on the uptake of rare earth elements on polyacrylamidoxime resins from natural concentrate leachate solutions, J. Dispersion Sci. Technol. 31 (2010) 1128–1135.
[76] F.Q. Ma, B.R. Dong, Y.Y. Gui, M. Cao, L. Han, C.S. Jiao, H.T. Lv, J.J. Hou, Y. Xue, Adsorption of low-concentration uranyl ion by amidoxime polyacrylonitrile fibers, Ind. Eng. Chem. Res. 57 (2018) 17384–17393.
[77] R. Janus, M. Wadrzyk, P. Natkanski, P. Cool, P. Kustrowski, Dynamic adsorption-desorption of methyl ethyl ketone on MCM-41 and SBA-15 decorated with thermally activated polymers, J. Ind. Eng. Chem. 71 (2019) 465–480.
[78] F. Wang, X.L. Wang, Y.J. Jiang, Z.W. Niu, W.S. Wu, H.X. Zhang, Study of adsorption performance and adsorption mechanism for U(VI) ion on modified polyacrylonitrile fibers, J. Radioanal. Nucl. Chem. 323 (2020) 366–377.
[79] D. Semitekolos, P. Kainourgios, C. Jones, A. Rana, E.P. Koumoulos, C.A. Charitidis, Advanced carbon fibre composites via poly methacrylic acid surface treatment; surface analysis and mechanical properties investigation, Compos. B 155 (2018)

237–243.
[80] C. Cannilla, G. Bonura, F. Frusteri, D. Spadaro, S. Trocino, G. Neri, Development of an ammonia sensor based on silver nanoparticles in a poly-methacrylic acid matrix, J. Mater. Chem. C 2 (2014) 5778–5786.
[81] F. Li, X. Li, P. Cui, Y. Sun, Plasma-grafted amidoxime/metal-organic framework composites for the selective sequestration of U(VI), Environ. Sci. Nano 5 (2018) 2000–2008.
[82] H. Chen, D.D. Shao, J.X. Li, X.K. Wang, The uptake of radionuclides from aqueous solution by poly(amidoxime) modified reduced graphene oxide, Chem. Eng. J. 254 (2014) 623–634.
[83] R. Cheng, M. Kang, S.T. Zhuang, L. Shi, X. Zheng, J.L. Wang, Adsorption of Sr(II) from water by mercerized bacterial cellulose membrane modified with EDTA, J. Hazard. Mater. 364 (2019) 645–653.
[84] P. Lignier, J. Estager, N. Kardos, L. Gravouil, J. Gazza, E. Naffrechoux, M. Draye, Swift and efficient sono-hydrolysis of nitriles to carboxylic acids under basic condition: Role of the oxide anion radical in the hydrolysis mechanism, Ultrason. Sonochem. 18 (2011) 28–31.
[85] D. Gregurec, N. Politakos, L. Yate, S.E. Moya, Strontium confinement in polyacrylic acid brushes: a soft nanoarchitectonics approach for the design of titania coatings with enhanced osseointegration, Mol. Syst. Des. Eng. 4 (2019) 421–430.
[86] R. Williams, pKa data (compiled by R. Williams), http://www.chem.wisc.edu/areas/reich/pkatable/pKa_compilation-1-Williams.pdf, Accessed: 4/6/2017.
[87] E.P. Serjeant, B. Dempsey, Ionisation constants of organic acids in aqueous solution. IUPAC Chemical Data Series, N° 23, Pergamon Press, Oxford; New York, 1979pp.
[88] N. Schüwer, H.-A. Klok, Tuning the pH sensitivity of poly(methacrylic acid) brushes, Langmuir 27 (2011) 4789–4796.
[89] A.M. El-Naggar, A.S. Emara, S.G.A. Alla, Effect of gamma irradiation on the metal sorption and separation of some divalent metals by some new polymeric bifunctional resins, J. Appl. Polym. Sci. 65 (1997) 1091–1101.
[90] Y. Marcus, Ion Properties, Marcel Dekker Inc, New York, NY, 1997, p. 259.
[91] M.V. Maslova, V.I. Ivanenko, L.G. Gerasimova, Effect of temperature on the kinetics of the sorption of strontium cations by a sorbent based on titanium phosphate, Russ. J. Phys. Chem. A 93 (2019) 1245–1251.
[92] S.M. Yakout, E. Elsherif, Investigation of strontium (II) sorption kinetic and thermodynamic onto straw-derived biochar, Part. Sci. Technol. 33 (2015) 579–586.
[93] A.M.S. Oancea, A.R. Popescu, M. Radulescu, V. Weber, E. Pincovschi, M. Cox, Kinetics of cesium and strontium ions removal from wastewater on gel and macroporous resins, Solvent Extr. Ion Exch. 26 (2008) 217–239.
[94] G.E. Boyd, B.A. Soldano, Self-diffusion of cations in and through sulfonated polystyrene cation-exchange polymers, JACS 75 (1953) 6091–6099.
[95] R.K. Bajpai, A.K. Gupta, M.G. Rao, Single particle studies of binary and ternary cation exchange kinetics, AlChE J. 20 (1974) 989–995.
[96] T.N. Ang, B.R. Young, M. Taylor, R. Burrell, M.K. Aroua, S. Baroutian, Breakthrough analysis of continuous fixed-bed adsorption of sevoflurane using activated carbons, Chemosphere 239 (2020) 124839.
[97] A. Shahbazi, H. Younesi, A. Badiei, Functionalized SBA-15 mesoporous silica by melamine-based dendrimer amines for adsorptive characteristics of Pb(II), Cu(II) and Cd(II) heavy metal ions in batch and fixed bed column, Chem. Eng. J. 168 (2011) 505–518.
[98] C. Araneda, C. Basualto, J. Sapag, C. Tapia, D. Cotorás, F. Valenzuela, Uptake of copper (II) ions from acidic aqueous solutions using a continuous column packed with microcapsules containing a β-hydroxyoximic compound, Chem. Eng. Res. Des. 89 (2011) 2761–2769.
[99] D.E. Chirkst, T.E. Litvinova, O.V. Cheremisina, M.V. Ivanov, N.A. Mironenkova, Isotherm of strontium sorption on clay, Russ. J. Appl. Chem. 76 (2003) 727–730.
[100] A. Ahmadpour, M. Zabihi, M. Tahmasbi, T.R. Bastami, Effect of adsorbents and chemical treatments on the removal of strontium from aqueous solutions, J. Hazard. Mater. 182 (2010) 552–556.
[101] Y.W. Chen, J.L. Wang, Removal of radionuclide Sr^{2+} ions from aqueous solution using synthesized magnetic chitosan beads, Nucl. Eng. Des. 242 (2012) 445–451.
[102] P. Cakir, S. Inan, Y. Altas, Investigation of strontium and uranium sorption onto zirconium-antimony oxide/polyacrylonitrile (Zr-Sb oxide/PAN) composite using experimental design, J. Hazard. Mater. 271 (2014) 108–119.
[103] B. Maranescu, A. Popa, L. Lupa, V. Maranescu, A. Visa, Use of chitosan complex with aminophosphonic groups and cobalt for the removal of Sr^{2+} ions, Sep. Sci. Technol. 53 (2018) 1058–1064.
[104] E. Karabayir, A. Ozdemir, B.F. Senkal, O.S. Taskin, A radioactively durable melamine-styrene based polymer: highly efficient removal of Sr-90, Appl. Radiat. Isot. 149 (2019) 96–103.
[105] R. Kumar, P. Malodia, M. Kachwaha, S. Verma, Adsorptive and kinetic studies of resin for removal of Cs^{+} and Sr^{2+} from aqueous solution, J. Water Chem. Technol. 41 (2019) 292–298.
[106] M. Xing, S.T. Zhuang, J.L. Wang, Adsorptive removal of strontium ions from aqueous solution by graphene oxide, Environ. Sci. Pollut. Res. 26 (2019) 29669–29678.
[107] Y. Wei, K.A.M. Salih, S. Lu, M.F. Hamza, T. Fujita, T. Vincent, E. Guibal, Amidoxime functionalization of algal/polyethyleneimine beads for the sorption of Sr(II) from aqueous solutions, Molecules 24 (2019) 3893.
[108] T. Abdollahi, J. Towfighi, H. Rezaei-Vahidian, Sorption of cesium and strontium ions by natural zeolite and management of produced secondary waste, Environ. Technol. Innovation 17 (2020) 100592.
[109] J. Liang, J. Li, X. Li, K. Liu, L. Wu, G. Shan, The sorption behavior of CHA-type zeolite for removing radioactive strontium from aqueous solutions, Sep. Purif. Technol. 230 (2020) 115874.